

UC Irvine

UC Irvine Electronic Theses and Dissertations

Title

Spin-Torque Assisted Microwave Detectors

Permalink

<https://escholarship.org/uc/item/9h97q9cp>

Author

Zhang, Jieyi

Publication Date

2017

Peer reviewed|Thesis/dissertation

UNIVERSITY OF CALIFORNIA,
IRVINE

Spin-Torque Assisted Microwave Detectors

DISSERTATION

submitted in partial satisfaction of the requirements
for the degree of

MASTER OF SCIENCE

in Physics

by

Jieyi Zhang

Dissertation Committee:
Professor Ilya Krivorotov, Chair
Professor Jing Xia
Professor Zuzanna Siwy

2017

DEDICATION

To my parents, Ming and Lingfeng.

TABLE OF CONTENTS

	Page
LIST OF FIGURES	iv
LIST OF TABLES	vi
ACKNOWLEDGMENTS	vii
ABSTRACT OF THE DISSERTATION	viii
1 Introduction and Background	1
1.1 Magnetization Dynamics	2
1.2 Giant and Tunneling Magnetoresistances	5
1.3 Spin Transfer Torque	8
1.4 Spin Torque Ferromagnetic Resonance	13
1.4.1 Conventional Ferromagnetic Resonance	14
1.4.2 Spin Torque assisted Ferromagnetic Resonance	16
2 Microwave Radiation Detector based on Spin Torque Diode Effect	19
2.1 Detector Design	20
2.2 Experimental Results	24
2.3 Discussion	32
3 Frequency Determination by a pair of Spin-Torque Microwave Detectors	36
3.1 Introduction	36
3.2 Theory	37
3.3 Experiment	42
3.4 Results and Discussion	43
4 Conclusion	49
Bibliography	51

LIST OF FIGURES

	Page
1.1 [1]Band structure for ferromagnet. Due to Stoner energy splitting, the majority and minority spins have different density of states at Fermi level.	6
1.2 [1]Spin-dependent resistance across a heterostructure. The structure consists of two FM layers separated by NMs. Left figure shows the parallel state (R_p), while the right one represents the anti-parallel state (R_{ap}). $R_1(R_2)$ is the resistance when electrons transmit through ferromagnet of the same(opposite) spin polarization. The interfacial resistance has been merged into the overall layer resistance in this case. It is clear that $R_{ap} > R_p$	6
1.3 Electrons interact with a ferromagnetic layer.	10
1.4 How spin torque acts in a magnetic multilayer heterostructure. FM1 and FM2 are the ferromagnetic layers. NM is the non-magnetic spacer in between two ferromagnetic layers. FM1 and FM2 represent the thicker fixed layer and the thinner free layer, respectively.	12
1.5 a. schematic diagram showing the direction of conservative torque (τ_H), the competition between spin transfer torque (τ_{st}) and damping torque (τ_d) during the magnetization precession; b. damped motion of magnetization at low current; c. steady state of oscillation at relatively higher current; d. switching process under high current. Figure from Ref.[2].	12
2.1 Schematic circuit diagram of an MTJ microwave detector. Part A: K-connector; part B: ESD protection circuit; part C: bias tee; part D: magnet with tunable position; part E: MTJ device; part F: coplanar waveguide antenna for receiving microwave signal.	21
2.2 Cross-sectional view of a coplanar waveguide showing relevant dimensions. The yellow section stands for the metal part of the coplanar waveguide. The grey part represents the dielectric substrate in the middle, which is made of Duroid.	25
2.3 Microwave detector layout design	25
2.4 Dimensions of the assembled microwave detector	26
2.5 Resistance vs field curve for a typical type A(a), and type B(b) MTJ device, with nominal lateral dimensions $160\text{ nm} \times 65\text{ nm}$ and $150\text{ nm} \times 70\text{ nm}$, respectively. Both fields are along in-plane hard axis.	27

2.6	Detector response to $P = +15$ dBm RF power: (a) Response of a type A detector. (b) Response of a type B detector. (c) Response of the best detector, a type B detector.	29
2.7	Response of a type B MTJ to a direct microwave input at -36 dBm power. .	31
2.8	Response of a type B detector under different applied field. Labels for each curve represent the distance between the MTJ and the magnet surface which is closer to the MTJ.	31
2.9	Response of a detector assembled with a pair of parallel MTJs (type B with $170 \times 70 \text{ nm}^2$ and $170 \times 60 \text{ nm}^2$ lateral dimensions) under different applied fields. The detector is placed under a horn antenna connected to a microwave generator, which outputs +15 dBm RF power. Labels for each curve represent the distance between the MTJ array and the magnet surface which is closer to the MTJ array.	32
2.10	Response of the same detector with a pair of parallel MTJs under the exact same condition after ESD protection test. Labels for each curve represent the distance between the MTJ array and the magnet surface which is closer to the MTJ array.	33
2.11	Response of the same detector with a pair of parallel MTJs under the exact same condition after vanish sealing and dropping test. Labels for each curve represent the distance between the MTJ array and the magnet surface which is closer to the MTJ array.	34
3.1	Schematic diagram of the amplitude-modulation ST-FMR setup.	41
3.2	Measured FMR signals (solid lines) and fitted curves (dashed lines) versus microwave drive frequency for three sets of detector arrays of different FL thicknesses: (a) $l = 3.0$ nm, (b) $l = 2.3$ nm, and (c) $l = 1.6$ nm. The insets show the determined frequency error Δf as a function of the drive frequency.	47
3.3	Frequency errors $\Delta f = f_{\text{det}} - f_{\text{real}} $ (color points) calculated from the determined frequency f_{det} [given by Eq. (3.4)] and real frequency f_{real} as a function of microwave drive frequency f_{real} for three studied cases of detector arrays: (a) orange squares, (b) violet circles, and (c) green triangles. The values of the detector's FMR linewidths for three detector arrays are indicated by color-coded solid (Γ_1) and dashed (Γ_2) horizontal lines, respectively. Black dash-dotted line is the theoretically calculated dependence Δf from Eq. (3.5) for the third detector array (c).	48

LIST OF TABLES

	Page
3.1 The FL thicknesses l , applied external fields $B_{\text{dc},1}$, $B_{\text{dc},2}$ and delivered microwave power P_{rf} for the three detector arrays studied in the experiment (see Fig. 3.2)	43
3.2 The resonance frequencies $f_{\text{res},1}$ and $f_{\text{res},2}$ (in GHz units), FMR linewidths Γ_1 and Γ_2 (in GHz units), and resonance volt-watt sensitivities $\varepsilon_{\text{res},1}$ and $\varepsilon_{\text{res},2}$ (in mV/mW units) calculated from the fitted curves shown in Fig. 3.2 for the three detector arrays studied in the experiment	44

ACKNOWLEDGMENTS

I would like to first express my deepest gratitude to my advisor Ilya Krivorotov. Without his thoughtful guidance and patience to my research projects, it would not be possible for me to fulfill my current research achievement. Following his sharp wisdom and insights in the study of physics, I really learned a lot of knowledge of physics and gained much capability on debugging and problem solving skills. It is such a valuable experience for me to be a graduate student in his group and will be a great treasure for my whole life.

I also would like to offer my thanks to my other committee members, Professor Jing Xia and Zuzanna Siwy for their time on reviewing my thesis and giving me helpful suggestions.

Additionally, I would like to thank all my lab mates in Krivorotov's group: Zheng Duan, Graham Rowlands, Brian Youngblood, Yu-Jin Chen, Andrew Smith, Igor Barsukov, Jenru Chen, Alejandro Jara, Han Kyu Lee, Chris Safranski. They have been offered me great amount of help during my research life.

I thank my parents Ming Zhang and Lingfeng Tan for all of their understanding and support. Finally, I want to express my deepest appreciation to my husband Zheng Duan, who has been assisting and encouraging me all the time.

ABSTRACT OF THE DISSERTATION

Spin-Torque Assisted Microwave Detectors

By

Jieyi Zhang

Master of Science in Physics

University of California, Irvine, 2017

Professor Ilya Krivorotov, Chair

This master dissertation investigates detection of microwave signals by magnetic tunnel junctions (MTJs) as sensing elements. The detection is based on the spin-torque diode effect. First, we show a wireless detection of microwave signals using a MTJ based detector. This MTJ detector is integrated with compact coplanar waveguide antennas and non-magnetic, microwave-transparent, reusable antenna holder. We compare the experimental results with MTJs of different magnetic layer structures. The tested structures can achieve comparable sensitivities to those of commercial semiconductor, diode-based microwave sensors. The detection frequencies can be tuned by a permanent magnet attached to the detector. Second, we demonstrate a microwave frequency determination method by a pair of MTJs as microwave detectors. A resonance-type spin-torque microwave detector (STMD) can be used to determine the frequency of an input microwave signal. But the accuracy is limited by the STMD's ferromagnetic resonance linewidth. By applying a pair of uncoupled STMDs connected in parallel to a microwave signal source, we show that the accuracy of frequency measurement is improved significantly.

Chapter 1

Introduction and Background

The magnetic tunnel junction (MTJ)[3, 4, 5, 6, 7, 8, 9] based spin-torque microwave detector (STMD)[10] relies on three fundamental properties of MTJs: (i) the tunneling magnetoresistance (TMR)[11, 6, 12, 13] effect, (ii) the spin-transfer torque (STT)[14, 15] effect and (iii) the spin-torque diode effect[16, 17]. The STT effect in magnetic multilayers can transfer spin angular momentum between magnetic layers separated by a thin non-magnetic spacer when electrical current is applied. Magnetization dynamics can be excited in the free magnetic layer (FL) of an MTJ structure by external microwave signal due to the transfer of spin angular momentum. The magnetization dynamics lead to oscillating resistance of the MTJ structure due to TMR effect, which furthermore generates a dc rectified voltage when coupled with the ac microwave current injected to the system. This phenomenon is the so called spin-torque diode effect[16, 17]. Because of this, MTJ becomes a very promising candidate for making nano-scale ultra-sensitive microwave detectors[10].

Chapter 2 will report the design of wireless STMD based on MTJ devices and discuss about the experimental results on detecting radiation microwave signals. MTJ devices have already been employed as sensing elements for microwave detections[18, 19, 20, 21, 22, 23]. Wireless

detection of microwave signals by MTJs has not been demonstrated yet. Compared to microwave signals confined in a transmission line, a radiated microwave signal decays rapidly. Thus, a MTJ device with relatively high microwave detection sensitivity is desirable. In addition, a special design of compact antenna is presented for the purpose of coupling microwave signals to MTJ device and improving the impedance match. Furthermore, a detector assembled with a pair of parallel MTJs will be shown, which is capable of detecting microwave signals of different frequency ranges (around 1 GHz and 2.7 GHz).

Chapter 3 presents a signal frequency determination method based on a pair of uncoupled STMDs connected in parallel to a microwave signal source, which dramatically reduces the frequency measurement error. For a single STMD, the frequency detection error is quite large and comparable to ferromagnetic resonance (FMR) linewidth (typically exceeding 100MHz) [16, 17, 20, 24]. Meanwhile, the detector's frequency operation range is also limited by this FMR linewidth of the single MTJ. In this work, we demonstrate that by employing a pair of uncoupled MTJs in parallel, the frequency detection error can be 2 - 5 times lower and the frequency operation regime is expanded about 3 times. The theoretical investigation on this phenomenon done in collaboration with Prof. Prokopenko will also be present.

1.1 Magnetization Dynamics

In the absence of any non-conservative torques, the overall energy of a small magnetic structure is governed by four energy terms:

$$E = E_{demag} + E_{exch} + E_{anis} + E_{ext} \quad (1.1)$$

where the four terms represent the energy contributions from demagnetizing field (E_{demag}), exchange (E_{exch}), anisotropy (E_{anis}), and any external fields (E_{ext}). The demagnetizing and exchange energies govern the competition between achieving minimal micromagnetic curvature and minimizing the magnetic charge accumulated at the sample boundaries. The exchange length defines the length scale over which the magnetization remains constant:

$$l_{exch} = \sqrt{\frac{2A}{\mu_0 M_s^2}} \quad (1.2)$$

where A is the exchange constant, μ_0 is permeability in vacuum, and M_s is the saturation magnetization of the sample. If the sample size becomes comparable or larger than l_{exch} , the system will undergo a transition toward to a non-uniform magnetization state. The anisotropy energy has many potential contributions: crystalline anisotropy, perpendicular anisotropy at the interface between certain materials, and exchange-induced anisotropy[25, 26, 13].

Based on the assumption that our system is uniformly magnetized, E can be expressed only as a function of the magnetization \vec{M} . The magnetization dynamics are governed by the Landau-Lifshitz (LL) or Landau-Lifshitz-Gilbert (LLG) equation[14]:

$$\frac{\partial \vec{M}}{\partial t} = -\gamma_L \vec{M} \times \vec{H}_{eff} - \frac{\alpha \gamma_L}{M_s} \vec{M} \times (\vec{M} \times \vec{H}_{eff}) \quad (LL) \quad (1.3)$$

$$\frac{\partial \vec{M}}{\partial t} = -\gamma_G \vec{M} \times \vec{H}_{eff} + \frac{\alpha}{M_s} \vec{M} \times \frac{\partial \vec{M}}{\partial t} \quad (LLG) \quad (1.4)$$

where γ_L and γ_G are the gyromagnetic constants similar to the gyromagnetic ratio γ , α is the constant damping term, \vec{H}_{eff} is the effective field which can be derived from Equation(1.1) :

$$\vec{H}_{eff} = -\frac{\partial E}{\partial \vec{M}} \quad (1.5)$$

Also, it can be easily proved that these two above equations are equivalent to each other by a modification of the gyromagnetic constants:

$$\gamma_G = (1 + \alpha^2)\gamma_L \quad (1.6)$$

Therefore, these two equations describe the identical magnetic dynamics. The first term represents the conservative torque by the effective field. The second term describes the damping torque caused by the energy lost during the magnetization precession. In the absence of any damping torque, the magnetization will process along conservative trajectories around the effective field \vec{H}_{eff} . When \vec{H}_{eff} only consists of an external field \vec{H}_{ext} , the precession trajectory of \vec{M} will be circular and with constant projection on \vec{H}_{eff} . This will occur only when the system has spherical symmetry. In real systems, any anisotropy can break the spherical symmetry, such as the shape anisotropy arising from the demagnetization field, which is given by the equation below.

$$\vec{H}_{demag} = -\underline{N} \cdot \vec{M} \quad (1.7)$$

where \underline{N} is the demag tensor. In systems with high-symmetry, such as thin cylindrical disks or ellipsoids, \underline{N} is diagonal, and therefore the shape anisotropy will lead to dynamics with a uniaxial or biaxial symmetry. When the damping torque is included, the magnetization vector will damp towards \vec{H}_{eff} – the energy minimum direction of the system.

1.2 Giant and Tunneling Magnetoresistances

Discovery of magnetoresistance enables a direct electrical read-out of the magnetization orientation, which provides substantial opportunities of application. The origin of magnetoresistance is due to the imbalanced populations of spin-up (\uparrow) and spin-down (\downarrow) electrons caused by the Stoner energy splitting in some 3d transition metal ferromagnets. Thus, for electrons incident into such a ferromagnetic layer, both the transport and scattering for spin-up (\uparrow) and spin-down (\downarrow) electrons are spin-dependent. Interfacial scattering due to different band structures is also one major contribution to this spin-dependent scattering process. If the ferromagnet has a band structure like figure 1.1 typical for 3d transition metal ferromagnets, spin-up (\uparrow) electrons will be the majority. In this case, the spin filter effect leads to a greater resistance for the incoming spin-down (\downarrow) electrons, which points to the opposite direction of the majority spins (\uparrow)[11, 27, 14].

Therefore, in a heterostructure composed of two ferromagnetic (FM) layers separated by non-magnetic (NM) spacers, the total resistance across the structure depends on the relative orientation of the magnetization vectors of the two FM layers[11, 3, 27]. Transport through this stack can be modeled as a network of resistors with parallel channels for spin-up and spin-down electrons shown in figure 1.2. When the magnetization of the two FM layers are aligned in parallel, the majority spin channel is the same in both ferromagnets and is therefore of lower resistance (R_p). Otherwise, when the FM layers are anti-parallel to each other, the system will be in a high resistance state (R_{ap}).

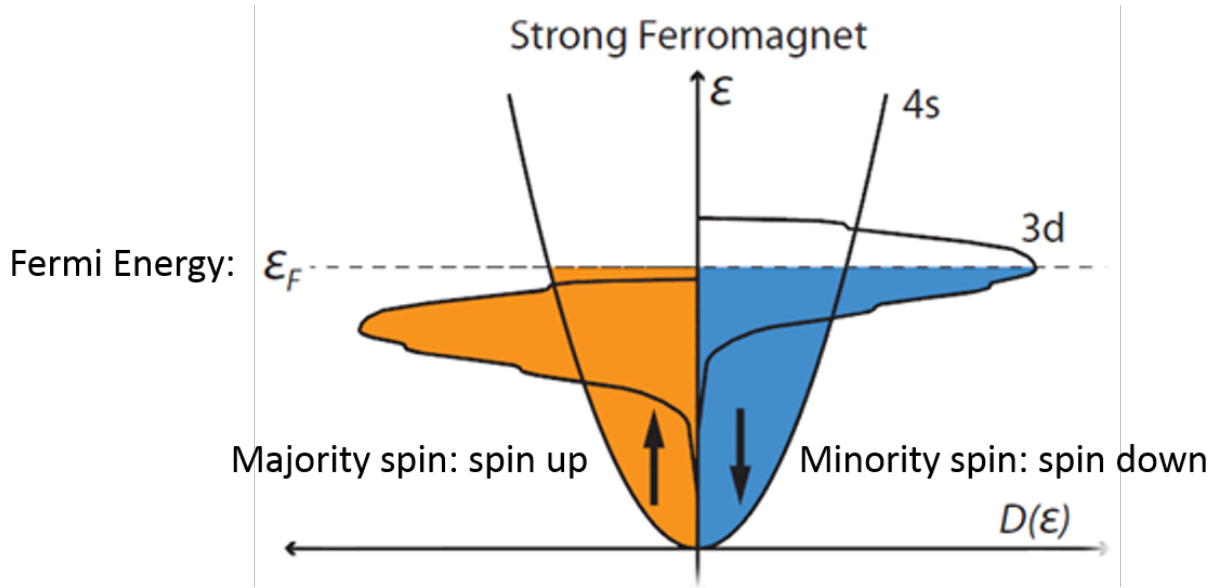


Figure 1.1: [1]Band structure for ferromagnet. Due to Stoner energy splitting, the majority and minority spins have different density of states at Fermi level.

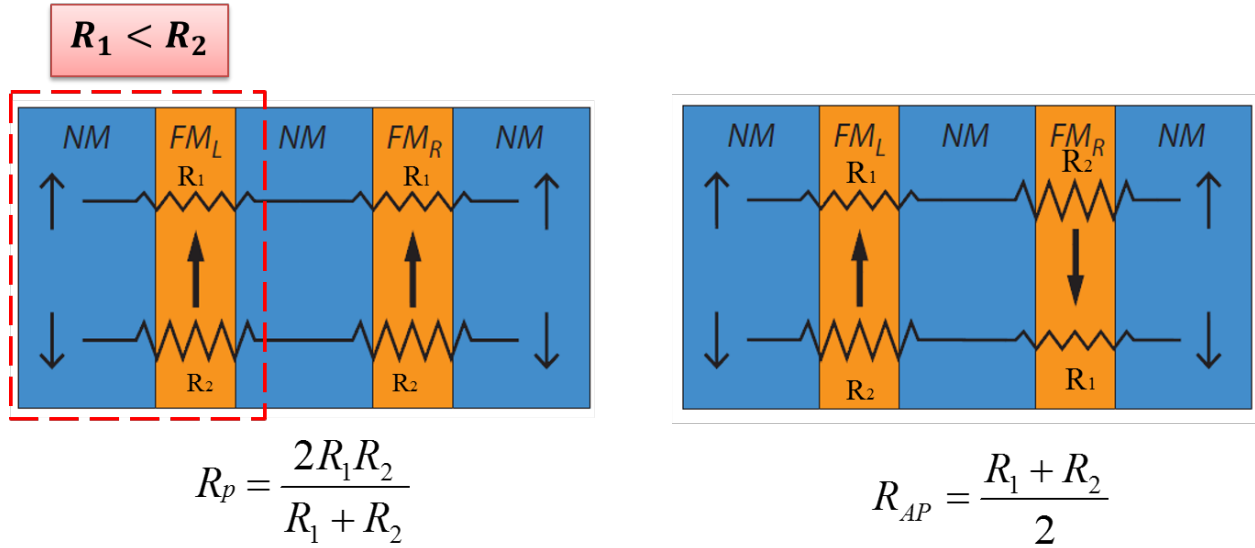


Figure 1.2: [1]Spin-dependent resistance across a heterostructure. The structure consists of two FM layers separated by NMs. Left figure shows the parallel state (R_p), while the right one represents the anti-parallel state (R_{ap}). R_1 (R_2) is the resistance when electrons transmit through ferromagnet of the same(opposite) spin polarization. The interfacial resistance has been merged into the overall layer resistance in this case. It is clear that $R_{ap} > R_p$.

In case that the NM spacer is metallic, this effect is referred as the giant magnetoresistance (GMR). It was first discovered in the current in-plane geometry[28, 29]. The full scale GMR value is defined as below:

$$\Delta R_{GMR} \equiv \frac{R_{ap} - R_p}{R_p} \quad (1.8)$$

GMR is typically on the order of tenths of a percent of the total resistance of samples in many materials. When the two magnetizations are in between parallel and anti-parallel state, the resistance of the structure in the current-perpendicular-to-plane geometry with any intermediate angle between the two magnetizations can be expressed by the angular dependence of GMR:

$$R = R_p + \Delta R_{GMR} \frac{\sin(\theta/2)^2}{1 + \chi \cos(\theta/2)^2} \quad (1.9)$$

where θ is the angle between the two magnetizations, and χ is a constant [30], which depends on layers' materials.

The motivation of looking for larger magnetoresistance drives the development of the heterostructure FM/NM/FM with a insulating barrier NM as the spacer. The tunneling magnetoresistance (TMR) was found in such magnetic tunnel junctions (MTJs). Originally this effect was observed across amorphous AlO_2 barriers, but later significantly larger TMR was found across MgO barrier with crystalline interface adjacent to FeCo electrodes[6, 12]. Compared to the previous metallic spin-valves, MTJs display much larger magnetoresistance and can achieve several hundred percent TMR at room temperature. The cause of the large MR

lies in band structure of this FeCo/MgO/FeCo multilayer sandwich. There is only one major tunneling channel through the particular Δ_0 band in Fe electrodes. The tunneling channels through other bands are strongly suppressed, resulting in a half-metallic like property of the MTJ[4, 5]. The angular dependence of the conductance across an MTJ has a simple cosine dependence:

$$G = G_0(1 + P^2 \vec{m} \cdot \vec{p}) \quad (1.10)$$

where G_0 is the average conductance, P describes the spin polarization efficiency. Meanwhile, MTJs also have some drawbacks from the application perspective, especially the relatively low break down voltage[31]. It is typically around 1.0 V. Due to the high resistance of MTJs, the critical current of the magnetization switching is always above or comparable to this break down level. Therefore, it does not satisfy all the ideal requirements for memory applications yet. However, MTJs are still believed to be one of the most promising candidates for the next generation of non-volatile memories . In addition, the high impedance of MTJs can cause difficulties in applications such as microwave communications, due to the poor impedance match to the surrounding electrical circuits.

1.3 Spin Transfer Torque

As one of the consequences of spin-dependent scattering first proposed by Slonczewski and Berger, electrons can transfer angular momentum to the ferromagnetic layer during the transmission process[14, 15]. When a charge current is injected to a ferromagnetic thin film, electrons will be either transmitted or reflected. Due to the band structure mismatch, electrons will undergo spin filtering process. As illustrated in figure 1.3, all the transmitted

electrons are spin-up (\uparrow) polarized, while the spin-down (\downarrow) electrons will be reflected. Such transmission/reflection process generates a spin polarized current. Electrons that enter the ferromagnet are subject to a huge exchange field and will precess around the magnetization. As different electrons travel along different paths in the ferromagnet, each electron would process at different angles when they exit the ferromagnet. By summing over electrons from the entire Fermi surface, the transverse components of the spins cancel out. Similar behavior also applies to the reflected electrons. As a consequence, the total polarization of the spin polarized current leaving the ferromagnet, summed over relevant states of the Fermi surface, is approximately collinear with the magnetization of the ferromagnetic layer. Thus, the entire transverse component of the spin current is absorbed at the interface, giving rise to reciprocal spin transfer torque (STT) exerted on this ferromagnet, which can alter the orientation of the magnetization[14].

As shown in the schematic diagram 1.4, when electric current interacts with ferromagnetic multilayers, the current will first be spin polarized by FM1 layer. It then carries spin angular moment to the second ferromagnetic layer (FM2) and becomes polarized along the direction of magnetization in FM2. In return, a spin transfer torque (STT) is exerted onto the second layer (FM2). Since FM2 layer is designed to be thinner (free layer), the magnetization of FM2 will be pulled towards the polarization direction of the current, same with the direction of FM1 (fixed layer). This procedure describes how a current going through a GMR structure alters the free layer's magnetization by spin transfer torque (STT).

The expression for this spin transfer torque is shown below[2]:

$$\vec{\tau}_{st} = -\beta(I)g(\theta)\vec{m} \times (\vec{m} \times \vec{p}) \quad (1.11)$$

where $\beta(I)$ represents the spin torque strength as a function of current, $g(\theta)$ describes the angular dependence arising from material properties of the heterostructure, and \vec{p} is the

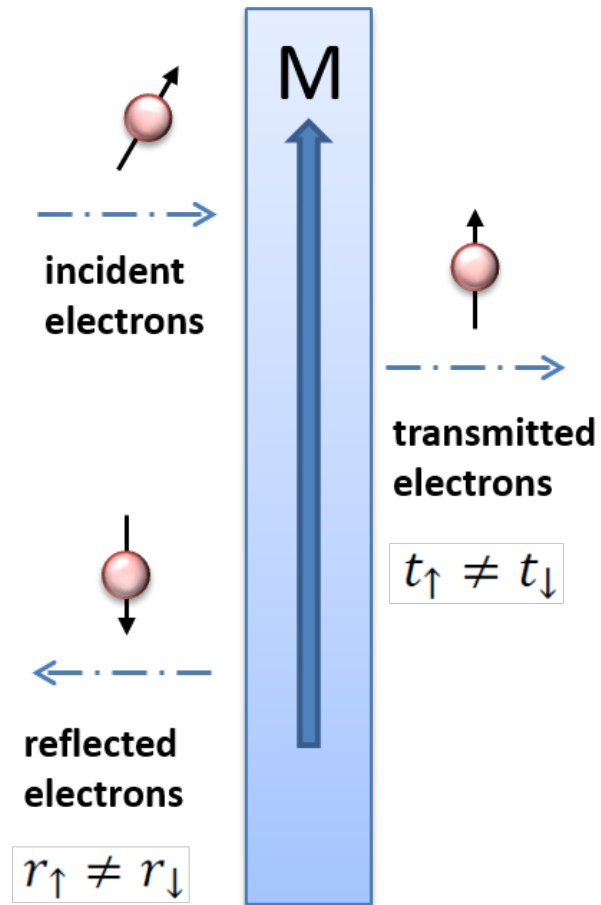


Figure 1.3: Electrons interact with a ferromagnetic layer.

normalized polarization vector. According to the equation above, the STT is an in-plane torque and perpendicular to the magnetic moment. Its amplitude is proportional to the current density[2].

It has also been demonstrated that an additional torque may arise from the spin accumulation, which has a similar expression to the torque given by from effective field:

$$\vec{\tau}_{fl} = -\beta'(I)g'(\theta)\vec{m} \times \vec{p} \quad (1.12)$$

where $\beta'(I)$ and $g'(\theta)$ have the same meanings as before. This field-like torque was observed to be negligibly small for metallic spin valves, however, its magnitude is generally much larger and plays a more important role in magnetic tunnel junctions[32, 33].

In reality, the dynamics of magnetization can be describe by the full version of LLG equation including the spin transfer torque[2]:

$$\frac{\partial \vec{M}}{\partial t} = -\gamma_G \vec{M} \times \vec{H}_{eff} + \frac{\alpha}{M_s} \vec{M} \times \frac{\partial \vec{M}}{\partial t} - \beta(I)g(\theta)\vec{m} \times (\vec{m} \times \vec{p}) \quad (1.13)$$

where the first term stands for the conservative field torque (τ_H), the second term is the damping torque (τ_d), and the third part represents the spin transfer torque (τ_{st}). The directions of these three torques are shown in figure 1.5(a).

In absence of any spin torque or damping, if the free layer's magnetization is perturbed away from \vec{H}_{eff} , it will begin processing around \vec{H}_{eff} . However, due to the existence of the damping torque in real samples, \vec{M} will always damp back towards the lowest energy

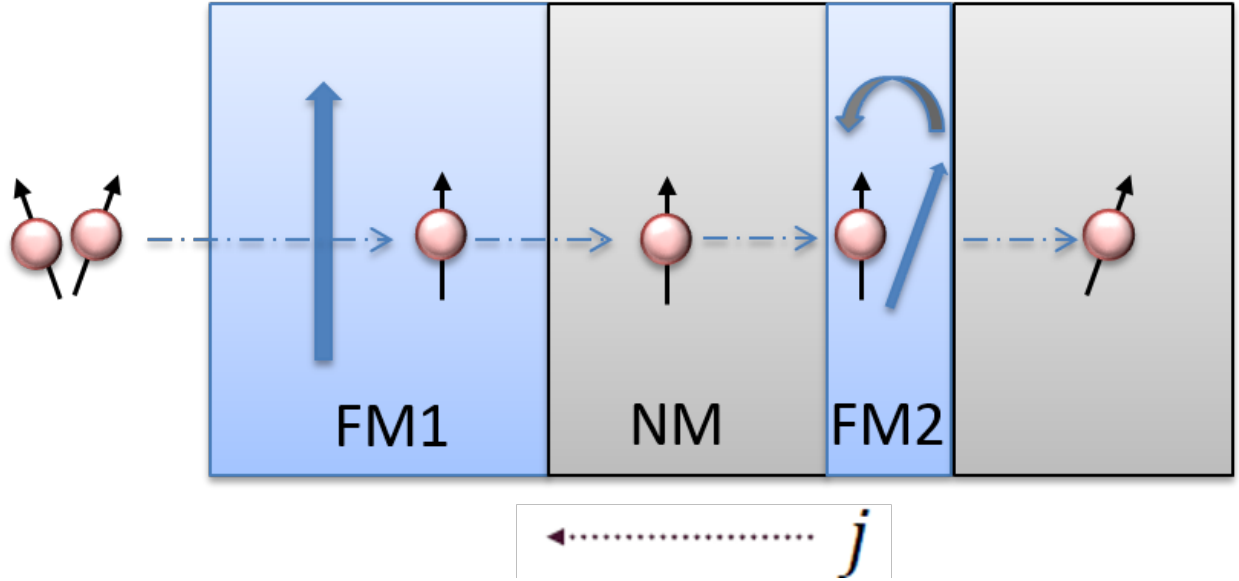


Figure 1.4: How spin torque acts in a magnetic multilayer heterostructure. FM1 and FM2 are the ferromagnetic layers. NM is the non-magnetic spacer in between two ferromagnetic layers. FM1 and FM2 represent the thicker fixed layer and the thinner free layer, respectively.

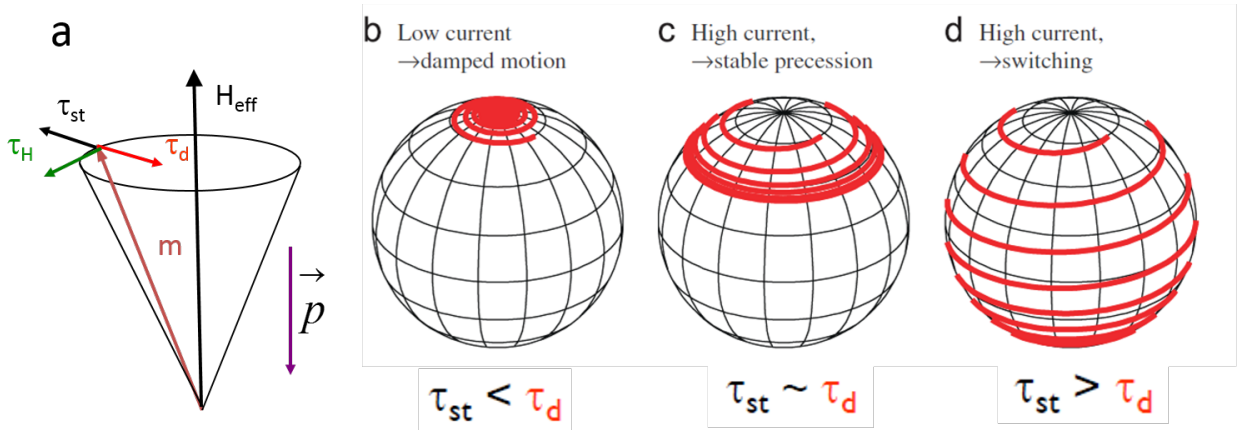


Figure 1.5: a. schematic diagram showing the direction of conservative torque (τ_H), the competition between spin transfer torque (τ_{st}) and damping torque (τ_d) during the magnetization precession; b. damped motion of magnetization at low current; c. steady state of oscillation at relatively higher current; d. switching process under high current. Figure from Ref.[2].

configuration along \vec{H}_{eff} [2].

When a charge current is applied, the direction of the spin transfer torque (STT) is either towards or opposite to the damping torque, depending on the current polarization. When the STT is parallel to the damping torque, the effective damping is enhanced by the applied current, therefore the magnetization will be pulled back more rapidly toward \vec{H}_{eff} . On the other hand, when the STT is anti-parallel to the damping torque, in case of a small applied current, the STT can only reduce the effective damping slightly, leading to a longer damping process till the magnetization reaches its equilibrium direction (shown in Fig. 1.5(b)). When the magnitude of the charge current reaches sufficiently high such that the spin transfer torque is comparable to or even larger than the damping torque, the magnetization will oscillate away from \vec{H}_{eff} following any perturbations and two possible dynamic states will occur depending on the strength of the spin transfer torque. The first scenario is when the STT is comparable to the damping torque, a steady precession state occurs (Fig. 1.5(c)). This phenomenon is called spin torque oscillation and was first found in experiments by Kiselev et al. in metallic spin valves [34], and subsequently by Rippard et al. in point contacts thin film composed of NiFe/Cu/CoFe [35]. The other possible state is the magnetization reversal, which occurs when the STT is much larger than the damping torque as illustrated in Fig. 1.5(d)[2]. The first experimental discovery of magnetization reversal was performed by Katine et al. in a Co/Cu/Co multilayer structure[36]. Later on, a large variety of magnetic nano-devices have been developed as one of the most promising candidates for the next generation of random access memories.

1.4 Spin Torque Ferromagnetic Resonance

So far, we have discussed how the LLG equation describes the magnetic precessional dynamics in a ferromagnet. As mentioned before, in absence of any damping-like torque, the

frequency of the magnetization precession is (for a spherical sample) given by the Larmor frequency $\omega = \gamma H_{eff}$ in the linear regime. Once the linear dynamics has been resonantly excited, this is what is referred to as ferromagnetic resonance (FMR) frequency. FMR can be detected via a number of approaches. We will discuss two of them in details in the following. The FMR spectra can provide deeper insight of the physics properties of the magnetic materials, such as the saturation magnetization, damping constant, magnetic anisotropy, sensitivity, spin-torque vector, etc..

1.4.1 Conventional Ferromagnetic Resonance

Most of the prior ferromagnetic resonance measurements were made by determining the microwave absorption of the ferromagnetic samples. This is so called the conventional ferromagnetic resonance[37]. Assuming there is a ferromagnetic ellipsoid placed in the Cartesian coordinate and a DC magnetic field applied along the longest axis (\hat{z}). The ferromagnetic ellipsoid is also exposed to microwave radiation, which produces RF magnetic field perpendicular to the DC field (along the \hat{x} axis). As discussed in the previous chapter, the RF magnetic field drives the magnetization to process around \vec{H}_{eff} . When the microwave frequency coincides with the eigenfrequency of the device, a large absorption of the microwave power would appear. The applied magnetic field can be expressed as follows:

$$\vec{H}_{app} = \hat{z}H_{DC} + \hat{x}H_{RF}e^{i\omega t} \quad (1.14)$$

Taking into account the demagnetization field in \vec{H}_{eff} , the x, y, z components of the effective magnetic field are:

$$H'_x = H_x - N_x M_x \quad (1.15)$$

$$H'_y = -N_y M_y \quad (1.16)$$

$$H'_z = H_z - N_z M_z \quad (1.17)$$

Ignoring any damping-like torques (they would not influence the resonance frequency significantly) and taking $H_x = \hat{x} \cdot \vec{H}_{app}$, $H_z = \hat{z} \cdot \vec{H}_{app}$, three orthogonal components of the LLG equation become:

$$\partial_t M_x = \gamma [H_z + (N_y - N_z) M_z] M_y \quad (1.18)$$

$$\partial_t M_y = \gamma [M_z H_x - (N_x - N_z) M_x M_z - M_x H_z] \quad (1.19)$$

$$\partial_t M_z \approx 0 \quad (1.20)$$

The resonant frequency can be obtained theoretically by solving the equations above:

$$\omega_0 = \gamma \sqrt{[H_z + (N_y - N_z) M_z][H_z + (N_x - N_z) M_z]} \quad (1.21)$$

In experiment, the microwave absorption can be measured by placing a ferromagnetic sample

in a microwave cavity under the drive of RF magnetic field. The microwave absorption is generally measured as a function of the applied external field, and the magnetic resonance can be determined from the peaks of the absorption curves. This technique has been adopted for the study of various magnetic properties, such as the saturation magnetization, the exchange constant, Gilbert damping, etc[38].

1.4.2 Spin Torque assisted Ferromagnetic Resonance

Spin transfer torque assisted ferromagnetic resonance(ST-FMR) [16, 17] is another technique recently developed for the study of magnetic properties. It is similar to the conventional FMR, except that the magnetization driving source is mainly the spin-torque instead of RF magnetic field produced by the microwave radiation. Briefly, when a microwave current is injected to a MTJ or spin valve, as discussed in the prior chapter, a microwave spin polarized current is induced and drives the free layer's magnetization precession, leading to an oscillating sample resistance caused by the magnetoresistance effect. A DC rectified voltage is therefore generated by averaging the product of this oscillating resistance and the ac current. The dependence of such a rectified voltage signal on the microwave drive frequency can be measured as the ST-FMR spectrum. Under a certain circumstance, the frequency of the external microwave drive coincides with the intrinsic frequency of the system, and a voltage peak appears in the measured ST-FMR spectrum. Detailed derivation is shown below:

$$R(t) = R_0 + \Delta R(t) = R_0 + Re(\sum_n \Delta R_{nf} e^{in2\pi ft}) \quad (1.22)$$

Then by Ohm's law

$$V_{dc} = \langle I_{rf} \cos(2\pi ft) R(t) \rangle = \frac{1}{2} I_{rf} |\Delta R_f| \cos(\delta_f) \quad (1.23)$$

where f is the driving frequency, δ_f is the phase difference between the ac resistance and driven current [16, 17].

In terms of DC bias (I, V) , V_{dc} can be approximated as [39]

$$\frac{1}{4} \frac{\partial^2 V}{\partial I^2} I_{rf}^2 + \frac{1}{2} \frac{\partial^2 V}{\partial \theta \partial I} \frac{\hbar \gamma_0 \sin \theta}{4eM_s \mathcal{V} \sigma} \times I_{rf}^2 (\varepsilon_{\parallel} S(\omega) - \varepsilon_{\perp} \Omega_{\perp} A(\omega)) \quad (1.24)$$

where

$$\varepsilon_{\parallel, \perp} = \left[\frac{2e/\hbar}{\sin(\theta)} \right] \frac{d\tau_{\parallel, \perp}}{dI} \quad (1.25)$$

are dimensionless differential torques, $S(\omega)$ and $A(\omega)$ are symmetric and anti-symmetric lorentzians given by

$$S(\omega) = \frac{1}{1 + \frac{(\omega - \omega_m)^2}{\sigma^2}} \quad (1.26)$$

$$A(\omega) = \frac{(\omega - \omega_m)}{\sigma} S(\omega) \quad (1.27)$$

Here, ω_m is the resonance precession frequency of the magnetization, $\Omega_{\perp} = \gamma(4\pi M_{eff} + H)/\omega_m$ in case of an elliptical thin film. σ is the line-width of the ST-FMR spectrum given by [39]

$$\sigma = \frac{\alpha \omega_m}{2} (\Omega_{\perp} + \Omega_{\perp}^{-1}) - \cot(\theta) \frac{\gamma \tau_{\parallel}(V, \theta)}{2M_s \mathcal{V}} \quad (1.28)$$

This equation reveals that the damping constant α can be obtained from ST-FMR measurement of the spectra line-width at $V = 0$:

$$\alpha_{eff} = \frac{2\sigma}{\omega_m(\Omega_{\perp} + \Omega_{\perp}^{-1})} \quad (1.29)$$

It is clear from equation (1.24) that by fitting the symmetric and antisymmetric components of an ST-FMR spectrum, one can obtain both the contributions from the in-plane and out-of-plane spin torque experimentally[39].

In ST-FMR measurement, usually we sweep the microwave frequency at a constant field when obtaining the spectra. Compared to the conventional absorptive FMR technique, one advantage of ST-FMR is that much smaller samples can be properly measured. The ST-FMR measurement on MTJs provides the foundation for the development of microwave detectors to be discussed in the following chapters.

Chapter 2

Microwave Radiation Detector based on Spin Torque Diode Effect

The microwave radiation detector discussed in this chapter is based on spin torque ferromagnetic resonance (ST-FMR)[16, 17]. Some prior work has explored the use of tunnel junctions as sensing elements [16, 18, 19, 20, 21, 22] using the spin torque diode effect. It has been shown that high detecting sensitivity has already been achieved[23], however, so far wireless detection of microwaves using a magnetic tunnel junction has not been demonstrated. It will be shown that the wireless microwave radiation detector discussed in this chapter has a relatively high sensitivity[18] comparable to a semiconductor diode and is designed to be frequency tunable by adjusting the magnet installed inside. Electrostatic discharge (ESD) protection and mechanical protection have also been implemented in order to make the detector ruggedized for normal use.

Unlike an electromagnetic signal confined in a transmission line (microwave waveguide, microwave cable, etc.), a radiated microwave signal decays quickly. As a result, in order to measure microwave radiation signal, a relatively sensitive detector should be implemented.

The control over source and cable impedances is possible when a source is connected directly to a detector, allowing improved impedance matching and better overall detection efficiency. However, the impedance of air is a constant so that some circuit optimization is required to couple microwave signals to the sensing element. The design presented in this chapter includes a compact antenna suitable for this purpose.

In this chapter I will describe the design of this microwave radiation detector and the characterization of detectors with two different types of tunnel junctions. We compared their sensitivities and demonstrated the frequency tunable function. Furthermore, a detector with a pair of two parallel MTJs is developed for enlarging the frequency detection range. The characterization result will also be discussed in this chapter. In this project, the formal group member Brian Youngblood designed the detector and ran the basic performance comparison between detectors with different types of MTJs. I have improved the ESD and mechanical protection onto the circuit of the detector. I also accomplished the demonstration of the frequency tunable function and the working detector with an MTJ array.

2.1 Detector Design

A schematic circuit diagram of the detector is given in Fig. 2.1. In our detector, we use MTJs with MgO barrier due to its large magnetoresistance[6, 12, 40]. The source of RF current is a coplanar waveguide (CPW) acting as an antenna, which is directly attached to the MTJ. The top lead of the MTJ is connected to the AC+DC port of a bias-tee while the DC port of the bias-tee is connected to the signal pin of a K-connector. The bottom lead of the MTJ is connected to the flange ground and the chassis of the detector. The DC voltage across the MTJ can be measured through the K-connector. The detector also includes an ESD protection circuit. A permanent magnet is affixed to a set screw to provide DC magnetic field.

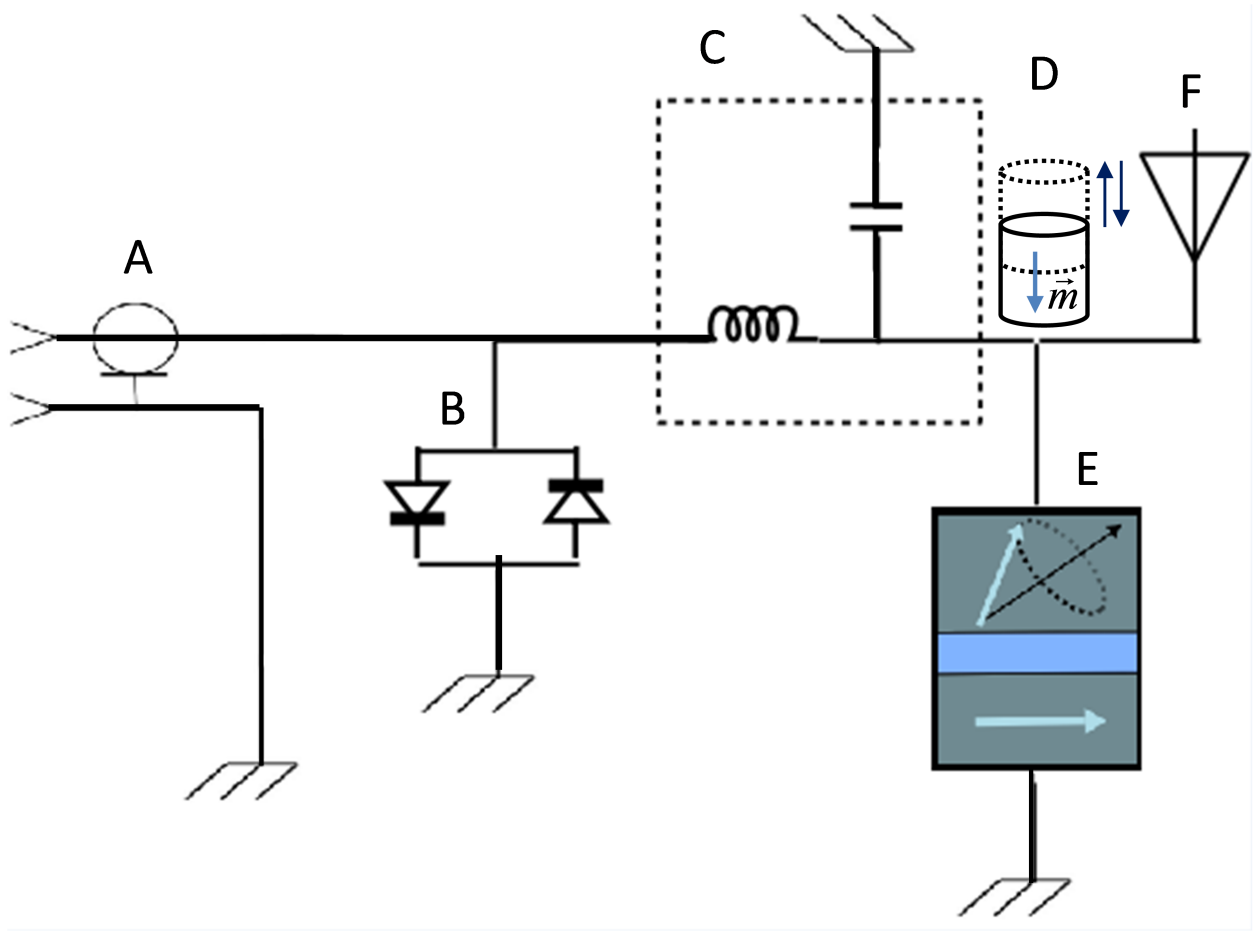


Figure 2.1: Schematic circuit diagram of an MTJ microwave detector. Part A: K-connector; part B: ESD protection circuit; part C: bias tee; part D: magnet with tunable position; part E: MTJ device; part F: coplanar waveguide antenna for receiving microwave signal.

The magnet inside provides a constant field that can be adjusted to obtain the best possible response from the magnetic tunnel junction and to tune the detection frequency range. The magnet is made from Nd₂Fe₁₄B (3.175 mm diameter \times 3.175 mm long) with a nominal surface field of 4 kG. The tunable position of the magnet provides a magnetic field range between 0 and 800 G applied at the MTJ. This range covers the fields which give the maximum response for the two types of detectors in our measurement.

The CPW makes the detector capable of picking up ambient microwave radiation (of the correct polarization) and, via the MTJ, converting it to a measureable DC voltage. It couples the microwave radiation to an input RF signal at the tunnel junction efficiently. This requires reasonably good matching between the impedance of CPW and that of air.

In an analytic model, a grounded CPW as depicted in Fig. 2.2 with a dielectric (ϵ_r) substrate of thickness $h \gg b = s + 2w$ has an impedance [41]:

$$\frac{60\pi}{\sqrt{\epsilon_{eff}}} \frac{1}{\frac{K(k)}{K(k')} + \frac{K(k_1)}{K(k'_1)}} \quad (2.1)$$

$$\epsilon_{eff} = \frac{1 + \epsilon_r \kappa}{1 + \kappa} \quad (2.2)$$

$$\kappa = \frac{K(k')}{K(k)} \frac{K(k_1)}{K(k'_1)} \quad (2.3)$$

$$k = s/b \quad (2.4)$$

$$k' = \sqrt{1 - k^2} \quad (2.5)$$

$$k_1 = \frac{\tanh(\pi s/4h)}{\tanh(\pi b/4h)} \quad (2.6)$$

$$k'_1 = \sqrt{1 - k_1^2} \quad (2.7)$$

As indicated by these equations, the characteristic impedance of the CPW is proportional to w and is inversely proportional to s . By modeling the coplanar waveguide structure in the finite element calculation software CST Microwave Studio, we were able to determine the parameters (s, w) showed in Fig. 2.2, which maximize the gain of the CPW antenna but still render the sample relatively easy to fabricate. For the 0.254 mm thick Duroid substrate we used, the optimal parameter set is $s = 0.2$ mm and $w = 0.1$ mm giving an impedance of 76Ω according to the modeling software. The impedance with the same dimension is 86Ω according to the analytical model. This discrepancy between numerical modeling and analytical approximation can be explained by the fact that our real CPW doesn't fulfill the condition $h \gg b$.

An additional feature of this detector is the ESD protection circuit designed to prevent damage to the delicate magnetic tunnel junction. The junction is susceptible to breakdown and becomes shorted across its thin insulating layer when exposed to relatively large transient voltages. The ESD protection circuit consists of two Schottky diodes connected in opposite directions which will shunt large voltages of either polarity to ground.

Fig. 2.3 shows the detailed design layout of our entire detector and the major dimensions are given by Fig. 2.4.

2.2 Experimental Results

For the detectors studied in this project, two different types of MTJs[6, 12, 40] were used, which will be referred to as type A and type B. Both are elliptical MgO tunnel junctions with CoFeB fixed and free layers. The layer structure is Substrate/buffers/SAF/MgO/FL. SAF refers to the synthetic anti-ferromagnet layer. FL is the free layer in the MTJ device. For type A junctions, the SAF is composed of PtMn(16)/Co₇₀Fe₃₀(2.5)/Ru(0.85)/Co₆₀Fe₂₀B₂₀(2.4), and the FL is Co₆₀Fe₂₀B₂₀(1.8) which is magnetized entirely in plane. The SAF structure for type B junctions is PtMn(15)/Co₇₀Fe₃₀(2.3)/Ru(0.85)/Co₄₀Fe₄₀B₂₀(2.4). The FL of type B junctions is composed of Co₂₀Fe₆₀B₂₀(1.8) which has partially out of plane magnetization. All thicknesses are given in nanometers. A type A junction has Co-rich free layer while type B is Fe-rich.

The resistance of most type A MTJs is between 300 Ω and 350 Ω at zero applied field. For type B junctions, resistances at zero applied field is higher, mostly ranging from 600 Ω to 620 Ω . Resistance vs. field plots for both types of junctions are shown in Fig. 2.5. The field is along the in-plane hard axis, which is the short axis of our elliptical device.

Tests on the full microwave detectors were run by placing the detectors at a set distance (approximately 18 cm) underneath a microwave horn antenna which was in turn connected to a microwave generator. The voltage signal was read by a Keithley 2182A nanovoltmeter which can measure down to 1 nV. This DC voltage was recorded as the frequency of the microwave emissions was varied. Fig. 2.6(a) shows the output voltage at the applied field giving the best signal for a typical detector with a type A tunnel junction patterned into

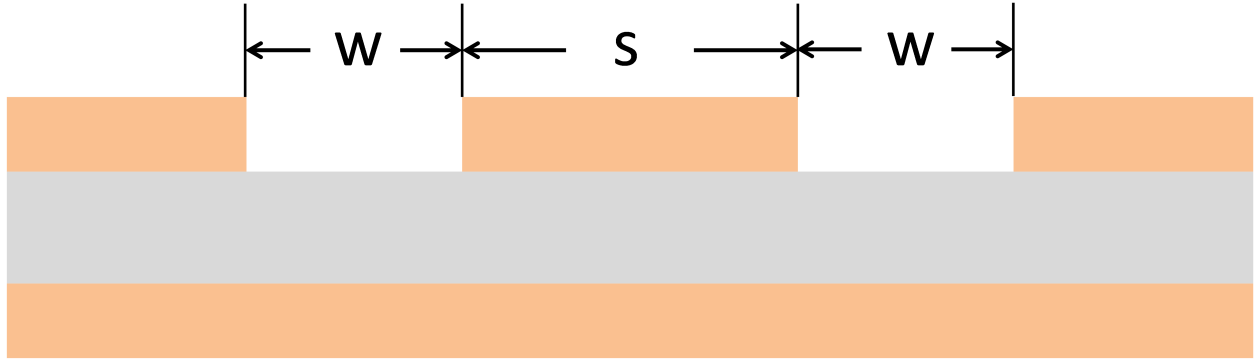


Figure 2.2: Cross-sectional view of a coplanar waveguide showing relevant dimensions. The yellow section stands for the metal part of the coplanar waveguide. The grey part represents the dielectric substrate in the middle, which is made of Duroid.

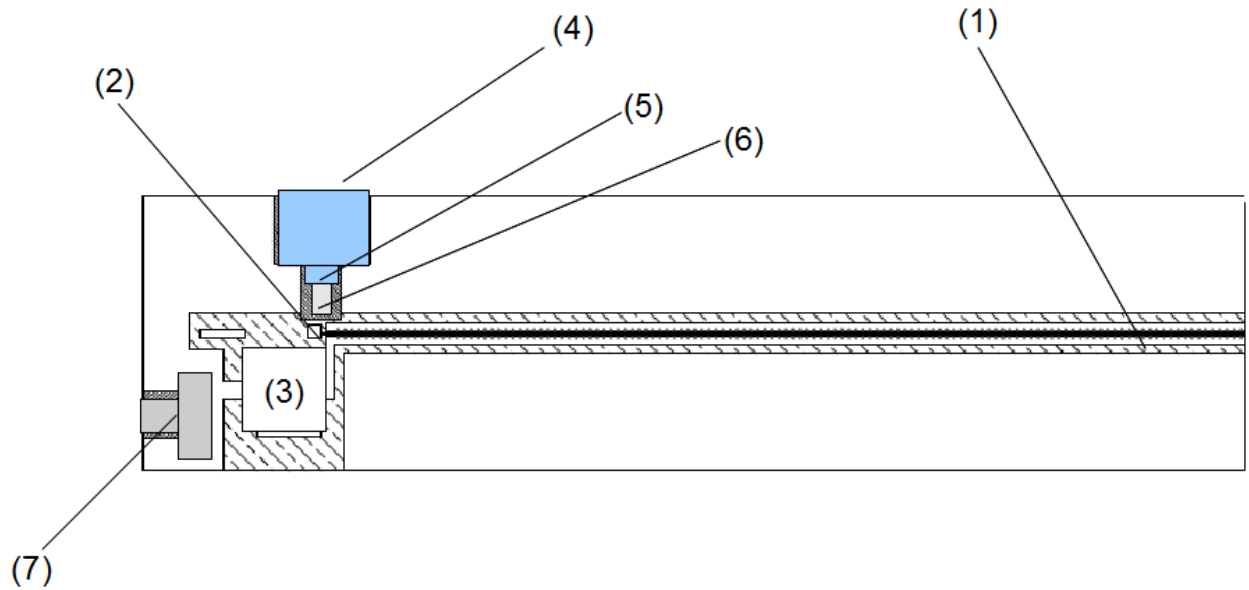


Figure 2.3: Microwave detector layout components: (1) Coplanar waveguide antenna, (2) MTJ device, (3) Bias-tee, (4) Brass screw holder, (5) Brass set-screw, (6) NdFeB magnet, (7) K-connector flange

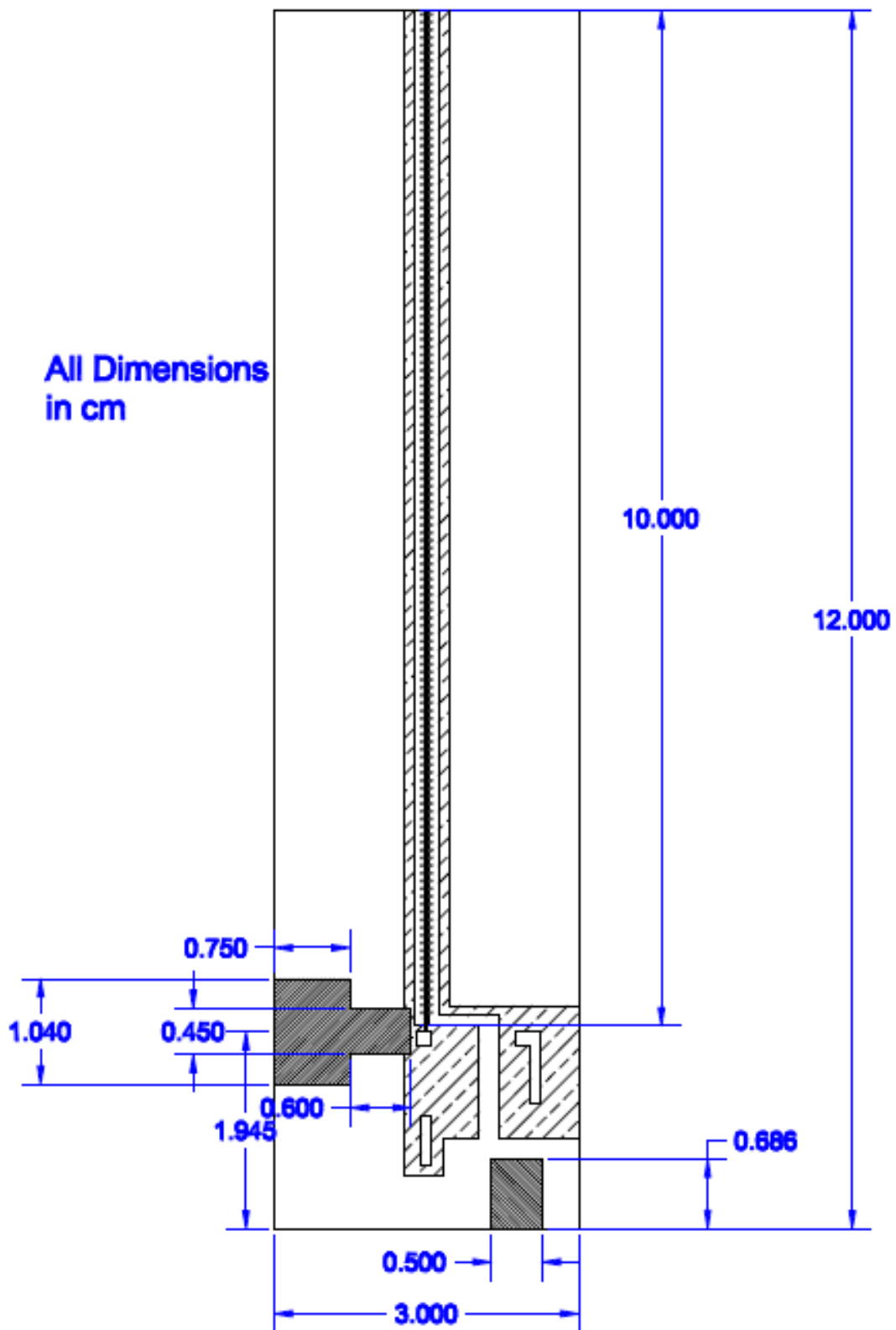


Figure 2.4: Dimensions of the assembled microwave detector

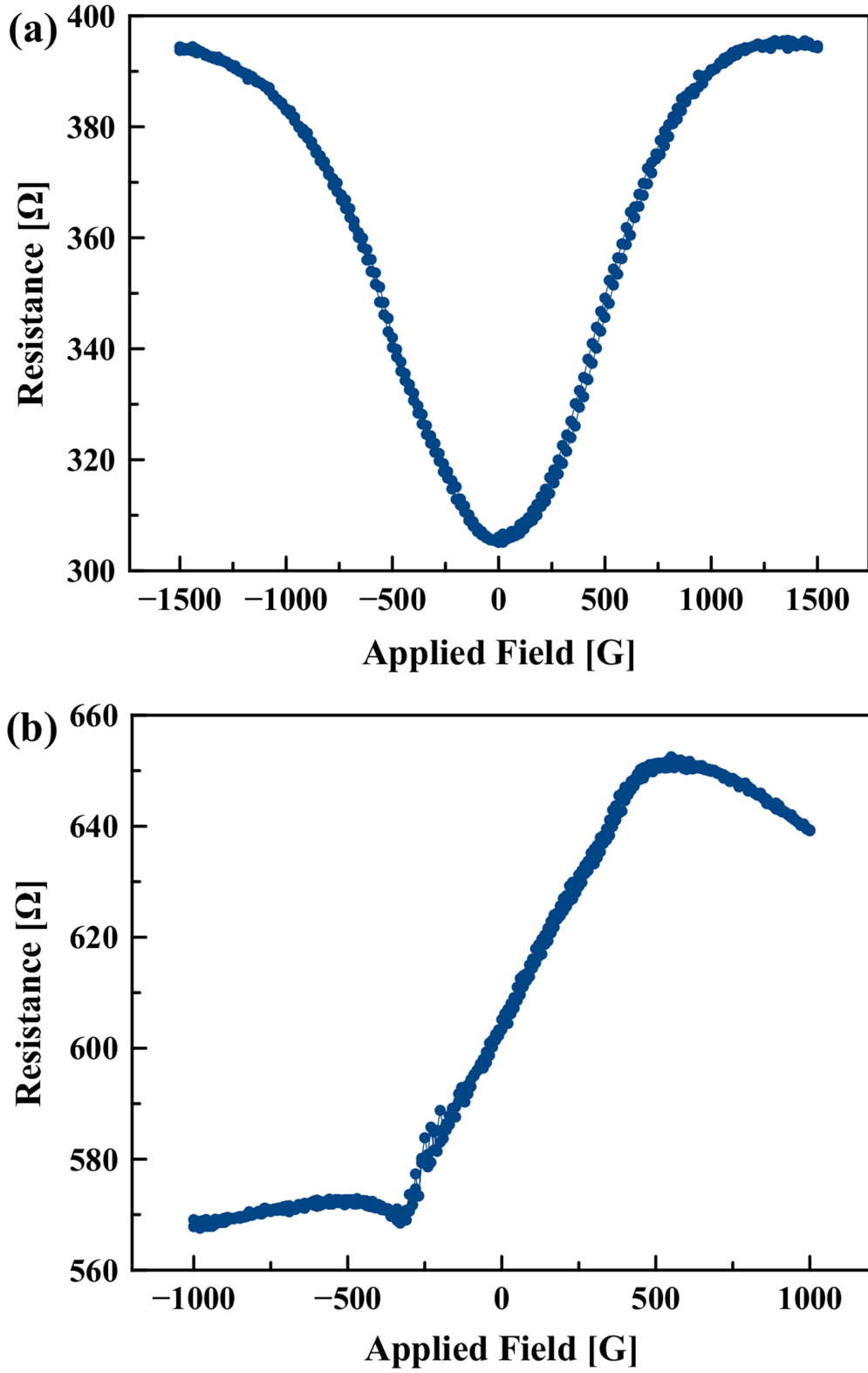


Figure 2.5: Resistance vs field curve for a typical type A(a), and type B(b) MTJ device, with nominal lateral dimensions $160 \text{ nm} \times 65 \text{ nm}$ and $150 \text{ nm} \times 70 \text{ nm}$, respectively. Both fields are along in-plane hard axis.

$160 \times 65 \text{ nm}^2$ elliptical nanopillar. This result was obtained with an external field of about 650 G along in-plane hard axis and a signal generator power output of 15 dBm.

Next, Fig. 2.6(b) shows the typical response of a type B detector. The output power from signal generator is also 15 dBm. Besides the stronger response of the type B detector, the best resonance is at a lower frequency for this kind of MTJ with a lower in-plane hard axis field of about 200 G, compared to fields at which the best response for type A samples occurs.

Fig. 2.6(c) shows the signal obtained from our best performing sample, which was of type B. As the figure shows, the response of this sample was atypically strong under the same generator output power and magnet position in Fig. 2.6(b), though the resonance frequency was the same as for other type B samples. This best performing sample was larger than the other type B samples tested, measuring $210 \text{ nm} \times 60 \text{ nm}$ while the other type B samples measured $150 \text{ nm} \times 70 \text{ nm}$. Also, since these tunnel junctions were designed to have equal resistance-area (RA) products regardless of size, the MTJ in the detector of Fig. 2.6(c) has a lower resistance (340Ω), closer to the impedance of the CPW antenna.

In order to calculate the sensitivity, we show in Fig. 2.7 the response of a type B sensing element ($150 \times 70 \text{ nm}^2$) under controlled conditions with the microwave power applied directly to the MTJ via a set of RF cables and a titanium probe. The RF power applied was -36 dBm and the applied field was 150 G along in-plane hard axis. The sensitivity is defined by the formula below:

$$\epsilon = \frac{V}{P_{inc}} \quad (2.8)$$

where V is the output voltage signal, while P_{inc} is the power applied onto the sample. Thus, the detector has a maximal sensitivity of 240 mV/mW when a power of $0.25 \mu\text{W}$ is applied. This is comparable to the best sensitivity for an MTJ-based detector reported to date[23] under zero bias. It is also on the same order with the sensitivity of the commercial diode we

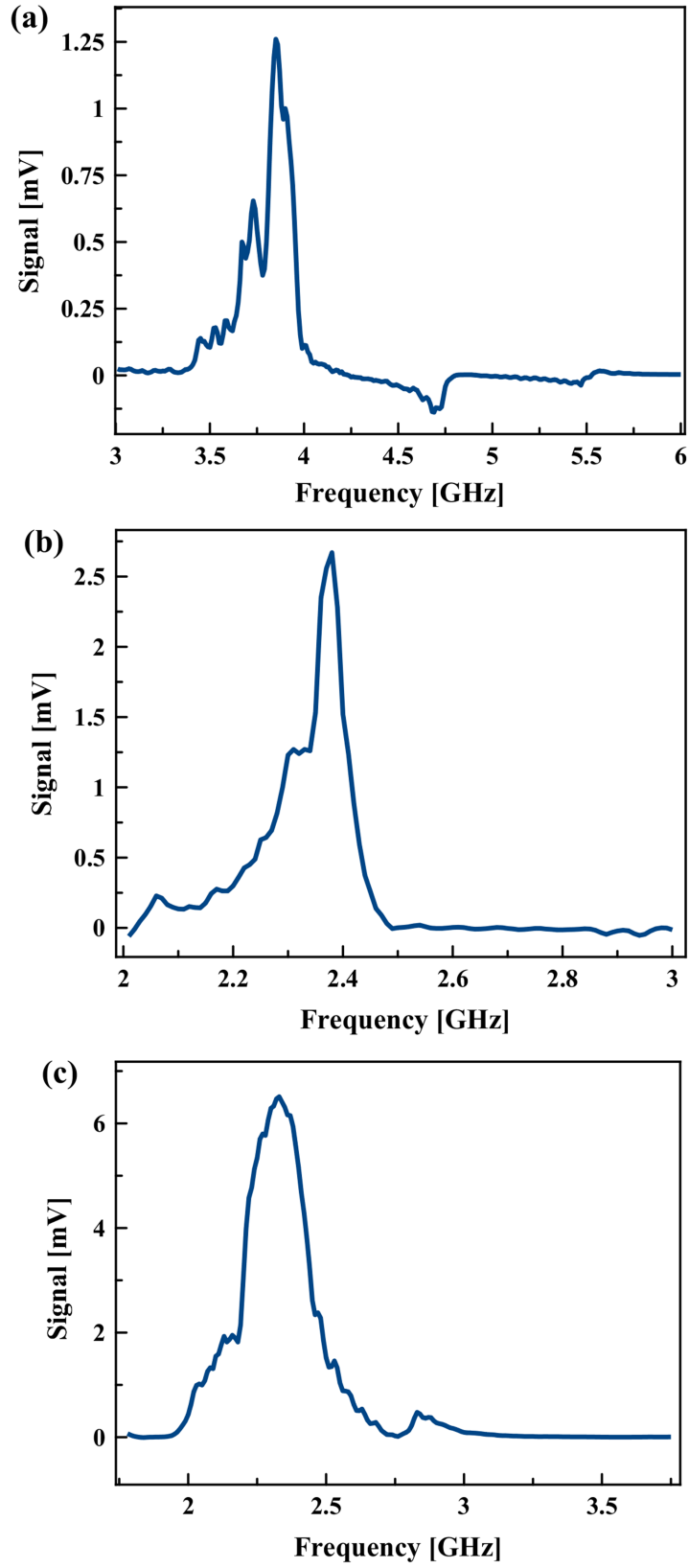


Figure 2.6: Detector response to $P = +15$ dBm RF power: (a) Response of a type A detector. (b) Response of a type B detector. (c) Response of the best detector, a type B detector.

used for calibration, which is quoted as 400 mV/mW.

Our detector is also a frequency tunable microwave detector. Fig. 2.8 shows the signal of a type B detector ($210 \times 60 \text{ nm}^2$) for radiated microwave signal as a function of applied field along the in-plane hard axis, which is provided by the attached magnet. By adjusting the position of the magnet, the resonance frequency of the detector can be tuned from 0.73 GHz to 1.28 GHz. The detection frequency range is determined by the intrinsic properties of each tunnel junction used for each detector.

Finally, we assembled a detector with two parallel tunnel junctions of different resonance frequency ranges. In this case, we show in fig.2.9 that we can detect microwave signals with two different frequencies at same time, which are around 1 GHz and 2.7 GHz. +15 dBm RF power provided by the microwave generator was delivered to the horn antenna. This type of detector fulfills the multi-range detecting function used to achieve by implementing two separate sensing elements. The resonance frequency can also be tuned by adjusting the inner magnet position, as described in fig.2.9. The resonance signal around 1 GHz is not as sensitive as the signal around 2.7 GHz. It is possibly due to the coupling between the microwave signals from the MTJ and that transmitted in the rest of the detector circuit. For the application purpose, reliability test on the ESD protection circuit and the mechanical protection (vanish seal on all wire bonds) has also been done as following. First, we applied 1 mA DC currents with different polarities to the input port of the detector, and then tested the detector performance. The results are shown in fig.2.10. No significant changes in characteristics were found after the ESD test. Second, we dropped the detector from three feet height after vanishing all the bonded wires. The performance after this mechanical test is given by fig.2.11. It demonstrates that no damage occurred to either the circuit holder or the detecting function of the detector.

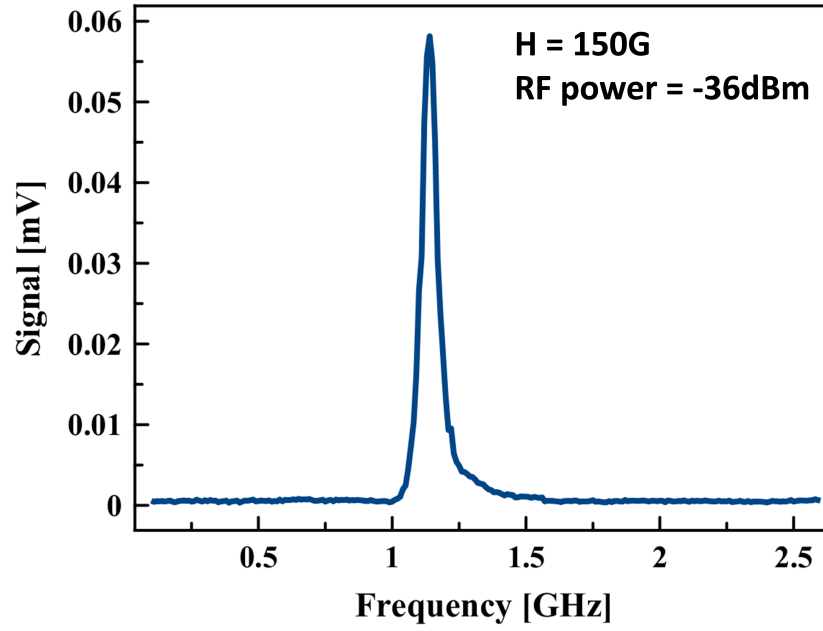


Figure 2.7: Response of a type B MTJ to a direct microwave input at -36 dBm power.

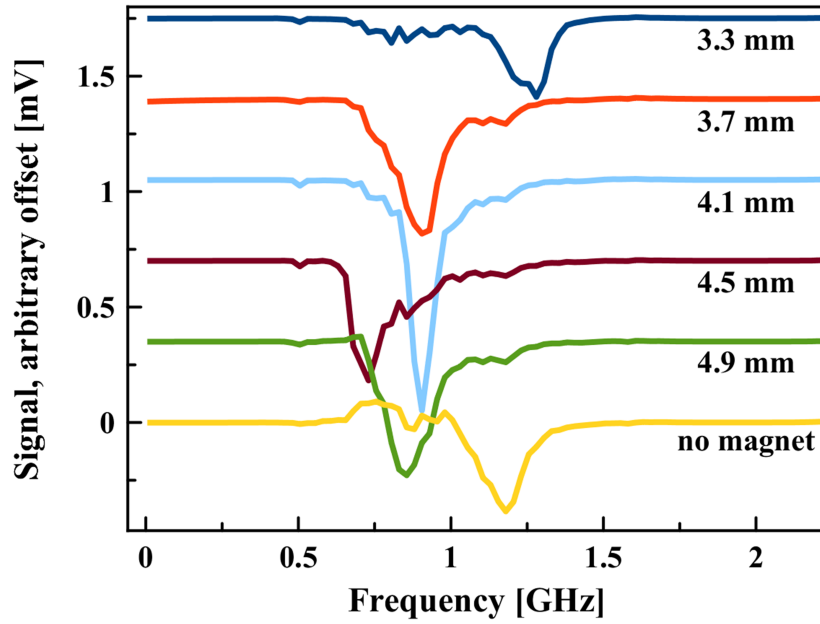


Figure 2.8: Response of a type B detector under different applied field. Labels for each curve represent the distance between the MTJ and the magnet surface which is closer to the MTJ.

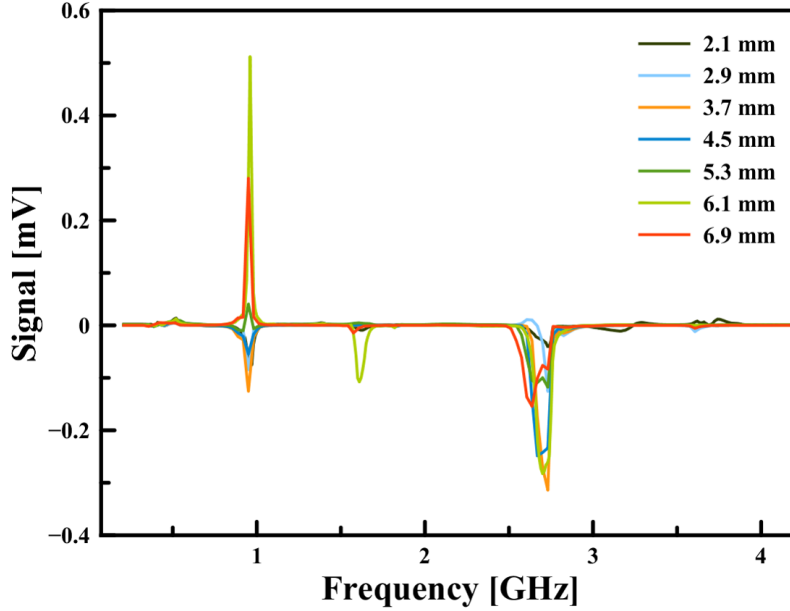


Figure 2.9: Response of a detector assembled with a pair of parallel MTJs (type B with $170 \times 70 \text{ nm}^2$ and $170 \times 60 \text{ nm}^2$ lateral dimensions) under different applied fields. The detector is placed under a horn antenna connected to a microwave generator, which outputs +15 dBm RF power. Labels for each curve represent the distance between the MTJ array and the magnet surface which is closer to the MTJ array.

2.3 Discussion

To explain why the type B MTJs have a stronger response we can examine Fig. 2.7 and note the asymmetry of the resonance peak. The asymmetric component of the spectrum is a signature of an out-of-plane torque[39]. Such an out-of-plane torque could cause the precession angle of the free layer magnetization to be larger, resulting in both a lower resonant precession frequency and a larger change in resistance which would result in a larger signal. The natural perpendicular-to-plane anisotropy of the type B junctions' free layers can achieve this effect. No such out-of-plane torque was observed in Ref. [39] for a non-biased system with in-plane magnetized free layer, though one is predicted in Ref. [42]. We will explain how this observable out-of-plane torque can arise at zero bias.

ST-FMR spectra obtained for other type B tunnel junction samples at various bias voltages

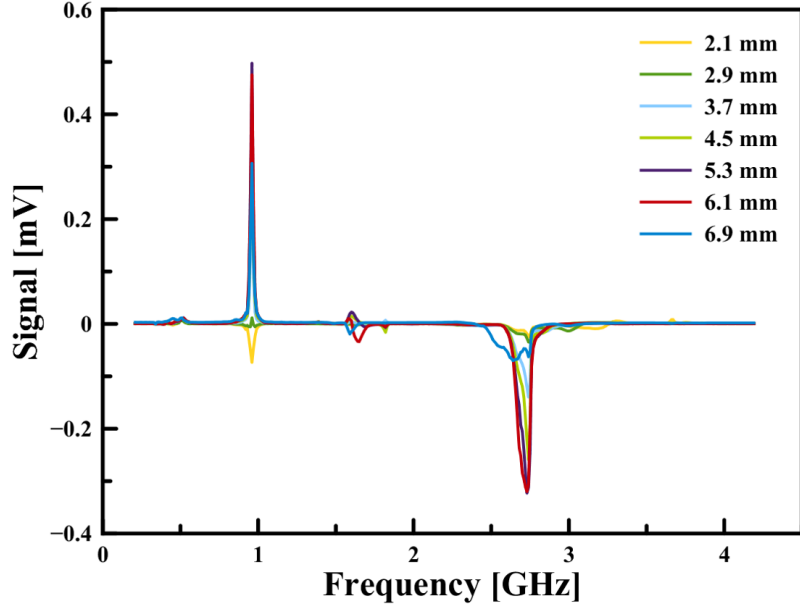


Figure 2.10: Response of the same detector with a pair of parallel MTJs under the exact same condition after ESD protection test. Labels for each curve represent the distance between the MTJ array and the magnet surface which is closer to the MTJ array.

indicate that the antisymmetric component of the peaks is the result of voltage induced magnetic anisotropy [43, 44, 13, 45, 46, 47], which is demonstrated in Ref. [48].

The RF voltage across the tunnel junction due to the oscillating RF current induces change of perpendicular anisotropy, resulting in an additive time-dependent term to \vec{H}_{eff} in the precession term of the Landau-Lifshitz-Gilbert equation for magnetization dynamics:

$$\partial_t \vec{M} = -\gamma_0 \vec{M} \times \vec{H}_{eff} \quad (2.9)$$

We can separate the contribution of voltage induced anisotropy from the rest of the effective field, which we label \vec{H}_{eff}^0 , giving

$$\partial_t \vec{M} = -\gamma_0 (\vec{M} \times \vec{H}_{eff}^0 + \vec{M} \times \vec{H}_{via} \sin(2\pi ft) \cos \theta) \quad (2.10)$$

Here, θ is the angle between the magnetizations of the free and pinned layers, and f rep-

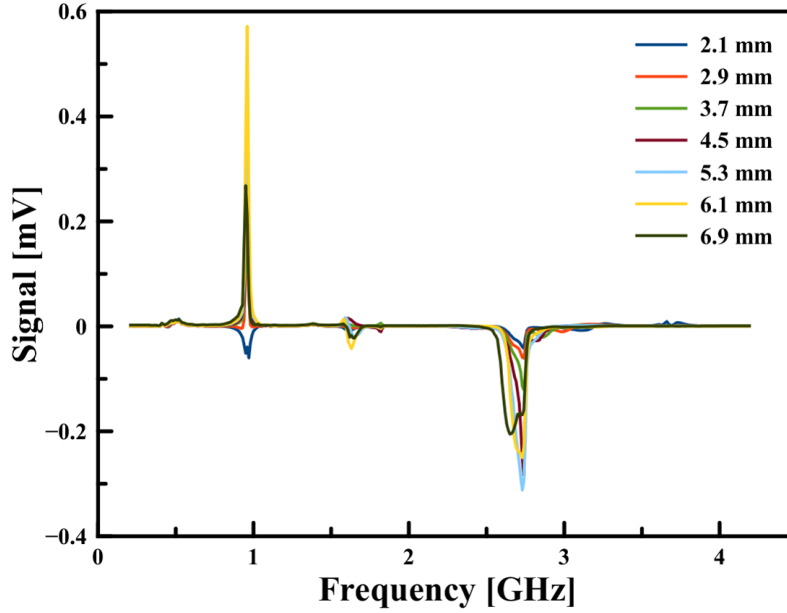


Figure 2.11: Response of the same detector with a pair of parallel MTJs under the exact same condition after vanish sealing and dropping test. Labels for each curve represent the distance between the MTJ array and the magnet surface which is closer to the MTJ array.

resents the frequency of RF voltage. The voltage induced contribution to the anisotropy is uniaxial, hence the factor of $\cos \theta = \hat{H}_{via} \cdot \hat{M}$ makes the contribution zero when the sample is magnetized in-plane. Equation (2.10) also shows us that this contribution is zero when the sample is magnetized completely perpendicular to the sample plane. The effect of voltage induced anisotropy is therefore important in MTJs with a significant component of magnetization perpendicular to the layer planes like our type B junctions. This torque due to voltage induced anisotropy change contributes to the antisymmetric part of the ST-FMR spectra. This out-of-plane torque is not field-like spin-torque, but the voltage induced anisotropy torque. Therefore, it appears at zero DC bias and is linear in applied DC bias to the extent that the out-of-plane anisotropy responds linearly to voltage.

In summary, we have demonstrated a compact, ruggedized, and ESD-protected microwave radiation detector based on magnetic tunnel junctions as sensing elements. Also, we show that the junctions' sensitivity (240 mV/mW) under zero bias approaches that of current

commercial semiconductor diode based detectors. In addition, this MTJ-based radiation detector has the feature of being intrinsically frequency tunable by adjusting the position of its magnet. We have also shown that tunnel junctions with free layers partially magnetized out of plane have enhanced sensitivity when compared to junctions with in-plane free layer. This enhancement is due to the voltage induced anisotropy. Furthermore, a more advanced detector based on two parallel MTJs has been demonstrated with the functionality of detecting microwave signals at two different ranges of frequencies. Reliability test on both the ESD and mechanical protection provided good feedback from the response of the detector.

For further improvement of the sensitivity, MTJs with partially perpendicular magnetized free layer are recommended to be implemented as sensing elements in active, dc biased detectors. Therefore, voltage induced anisotropy will play as a greater role and damping can be reduced due to the current induced spin transfer torque[23] in the MTJ device. Besides improvements to the MTJ sensing elements, impedance matching circuits can also be applied to optimize the impedance match between air, antenna, and the sensing element in the detector. Following the suggestions above, a microwave detector with a much larger sensitivity could possibly be achieved in the future.

Chapter 3

Frequency Determination by a pair of Spin-Torque Microwave Detectors

3.1 Introduction

This work was done in collaboration with professor Prokopenko, who proposed the concept of using a pair of MTJ detectors for microwave frequency measurements and performed theoretical analysis. My contribution is experimental realization of the MTJ-based microwave frequency meter and the corresponding data analysis. In typical experiments [16, 17, 20, 23, 49] spin-torque microwave detector (STMD) operates in the dynamic regime, where the spin transfer torque (STT) excites a small-angle magnetization precession about the equilibrium direction of magnetization in the free layer (FL) of an MTJ (description of the other possible non-resonance operation regime of an STMD is not considered in this work and can be found in [24, 50, 21, 10]). In this regime the detector operates as a frequency-selective, quadratic microwave detector with a resonance signal frequency f that is close to the ferromagnetic resonance (FMR) frequency f_{res} of the FL. The rectified dc voltage U_{dc}

generated by an STMD is directly proportional to the input microwave power P_{rf} , while the detector's frequency operation range has an order of the FMR linewidth Γ (here and below specified in frequency units) [16, 17, 20, 23, 49]. This makes an STMD a natural microwave frequency detector at frequencies that are close to the resonance frequency f_{res} . However, such a device has many limitations preventing its wide application in microwave technology: (i) a valid frequency detection by an STMD is only possible for input microwave signals of known power P_{rf} only, (ii) the detection procedure is not completely unambiguous and gives two possible frequency values, (iii) the STMD's frequency detection error Δf is quite large and comparable to the FMR linewidth Γ , which in typical experiments can exceed 100 MHz [16, 17, 20, 24, 51], (iv) the detector's frequency operation range is also limited by the FMR linewidth Γ .

This work introduces a simple and unambiguous method of the determination of a microwave signal frequency. The method is based on the application of two uncoupled STMDs connected in parallel to a microwave signal source and can be easily realized experimentally even for the signals of unknown microwave power. We show theoretically and experimentally that such pair of STMDs can act as a high-efficiency microwave frequency detector having substantially reduced frequency determination error Δf (2–5 times less) and greatly expanded frequency operation range and thereby it may overcome the limitations of the frequency detector based on a single STMD.

3.2 Theory

So far, a single STMD has been applied for determining frequencies of microwave signals. The absolute value of a rectified output dc voltage U_{dc} (neglecting the phase relations between the input microwave signal and magnetization oscillations in the FL) of a resonance-type

quadratic STMD is given by [18, 10, 16]

$$U_{\text{dc}} = \varepsilon_{\text{res}} P_{\text{rf}} \frac{\Gamma^2}{\Gamma^2 + (f - f_{\text{res}})^2}. \quad (3.1)$$

Here P_{rf} is the input microwave power, f_{res} and Γ are the FMR frequency and FMR linewidth, respectively, and ε_{res} is the resonance volt-watt sensitivity of an STMD defined as $U_{\text{dc}}/P_{\text{rf}}$ at $f = f_{\text{res}}$. In [18] ε_{res} is predicted to be approximately 10^4 mV/mW for a passive (no dc bias) STMD, while the best experimental value achieved to date is $\varepsilon_{\text{res}} = 630$ mV/mW for a conventional unbiased STMD [23] and $\varepsilon_{\text{res}} = 970$ mV/mW for a passive detector based on MTJ having a voltage-controlled interfacial perpendicular magnetic anisotropy of the FL [49]. The resonance volt-watt sensitivity of an STMD can be greatly enhanced by applying a dc bias current to the detector sufficiently large to compensate the natural damping in the FL of an MTJ. Recent experiments show that such dc-biased STMDs may have the resonance volt-watt sensitivity of $\varepsilon_{\text{res}} \approx 1.2 \cdot 10^4$ mV/mW [23] and $\varepsilon_{\text{res}} \approx 7.4 \cdot 10^4$ mV/mW [49]. These values of the resonance volt-watt sensitivity ε_{res} of an STMD are comparable to (passive detector) or greater than (dc-biased detector) the volt-watt sensitivity of a semiconductor Schottky diode.

According to Eq. (3.1) the frequency f of an input microwave signal can be determined by measuring the output dc voltage of the detector U_{dc} if the input microwave power P_{rf} , the detector's resonance volt-watt sensitivity ε_{res} , its resonance frequency f_{res} and FMR linewidth Γ are known:

$$f = f_{\text{res}} \pm \Gamma \sqrt{\frac{\varepsilon_{\text{res}} P_{\text{rf}} - U_{\text{dc}}}{U_{\text{dc}}}}. \quad (3.2)$$

Typically the last three parameters, ε_{res} , f_{res} and Γ , can be measured experimentally or calculated theoretically for a particular detector prior to the measurement of the input microwave signal frequency f . However, even for the signal of known microwave power P_{rf}

and arbitrary frequency $f \neq f_{\text{res}}$ it is impossible to clearly determine the frequency f from the solution (3.2) of the second-order Eq. (3.1) using only *one* measured value – the detector’s output dc voltage U_{dc} . Although this problem could be solved by selecting a particular work frequency range of the detector ($f < f_{\text{res}}$ or $f > f_{\text{res}}$) and/or by using an additional low-pass ($f < f_{\text{res}}$) or high-pass ($f > f_{\text{res}}$) microwave filter for input microwave signal subjected to the detector, it also seriously affects the complexity and cost of the entire device. Regardless of whether the microwave filter is used or not, the frequency determination error Δf in this case is significant, because it is comparable to the FMR linewidth Γ that can exceed 100 MHz in typical experiments [16, 17, 20, 24, 51]. In addition, the single STMD method of frequency determination becomes unacceptable if the power P_{rf} of the input microwave signal is unknown.

Here we propose a simple model of the microwave frequency detector consisting of two uncoupled resonance-type quadratic STMDs [10, 16, 17, 20, 23, 49]. In general, we assume that the detectors have different volt-watt sensitivities $\varepsilon_{\text{res},1}$ and $\varepsilon_{\text{res},2}$, the resonance frequencies $f_{\text{res},1}$ and $f_{\text{res},2}$, and the FMR linewidths Γ_1 and Γ_2 (here parameters of the first and second detectors are labeled by indexes 1 and 2, respectively). Considering each STMD as an independent device, the output dc voltages generated by the detectors, $U_{\text{dc},1}$ and $U_{\text{dc},2}$, can be written similarly to Eq. (3.1) as

$$\begin{aligned} U_{\text{dc},1} &= \varepsilon_{\text{res},1} P_{\text{rf},1} \frac{\Gamma_1^2}{\Gamma_1^2 + (f - f_{\text{res},1})^2}, \\ U_{\text{dc},2} &= \varepsilon_{\text{res},2} P_{\text{rf},2} \frac{\Gamma_2^2}{\Gamma_2^2 + (f - f_{\text{res},2})^2}, \end{aligned} \tag{3.3}$$

where $P_{\text{rf},1}$ and $P_{\text{rf},2}$ are the input microwave powers acting on the first and second detector, respectively. We can assume that the detectors are located quite close to each other (the distance between them should be much smaller than the wavelength of detected microwave signal), but the coupling between the detectors remains negligible. We also assume that the detectors are connected in parallel to a microwave signal source and their microwave

impedances are approximately equal. In this case, the input microwave power applied to each detector is the same: $P_{\text{rf},1} = P_{\text{rf},2} = P_{\text{rf}}$. Using these assumptions, the input microwave powers $P_{\text{rf},1}$ and $P_{\text{rf},2}$ can be eliminated from Eq. (3.3) and the equation for the frequency f of the input microwave signal could be written in the form:

$$f = \frac{\kappa f_{\text{res},1} - f_{\text{res},2} + \sqrt{(\kappa - 1)(\Gamma_2^2 - \kappa \Gamma_1^2) + \kappa \Delta f_{\text{res}}^2}}{\kappa - 1}. \quad (3.4)$$

Here, we assume that $f_{\text{res},2} > f_{\text{res},1}$, and introduce a dimensionless variable $\kappa = (U_{\text{dc},1}/U_{\text{dc},2})(\varepsilon_{\text{res},2}/\varepsilon_{\text{res},1})(\Gamma_2/\Gamma_1)^2$, which can be easily calculated for a particular set of detectors and use ansatz $\Delta f_{\text{res}} = f_{\text{res},2} - f_{\text{res},1} > 0$. The presented solution (3.4) is unique in the frequency range $f_{\text{res},1} \leq f \leq f_{\text{res},2}$ and can be used for the determination of unknown frequency f of the input microwave signal from the measured voltages $U_{\text{dc},1}$, $U_{\text{dc},2}$ and known detector's parameters $(\varepsilon_{\text{res},1}, \varepsilon_{\text{res},2}, f_{\text{res},1}, f_{\text{res},2}, \Gamma_1, \Gamma_2)$. This solution is valid for the case $\kappa \neq 1$, i.e. when we have detectors with different working parameters. Otherwise, in the case $\kappa = 1$, expression (3.4) transforms to $f = 0.5(f_{\text{res},2} + f_{\text{res},1}) + 0.5(\Gamma_2^2 - \Gamma_1^2)/\Delta f_{\text{res}}$ and becomes almost equivalent to the solution (3.2) for a single STMD.

If we consider the detector's parameters $\varepsilon_{\text{res},1}, \varepsilon_{\text{res},2}, f_{\text{res},1}, f_{\text{res},2}, \Gamma_1, \Gamma_2$ as frequency-independent values (at least in the frequency range $f_{\text{res},1} \leq f \leq f_{\text{res},2}$), the expression for the frequency error Δf can be estimated from Eq. (3.4) as:

$$\Delta f = \sqrt{\left(\frac{\partial f}{\partial U_{\text{dc},1}}\right)^2 \Delta U_{\text{dc},1}^2 + \left(\frac{\partial f}{\partial U_{\text{dc},2}}\right)^2 \Delta U_{\text{dc},2}^2} = \frac{\kappa}{2(\kappa - 1)^2} \frac{|Q|}{S} \sqrt{\left(\frac{\Delta U_{\text{dc},1}}{U_{\text{dc},1}}\right)^2 + \left(\frac{\Delta U_{\text{dc},2}}{U_{\text{dc},2}}\right)^2}. \quad (3.5)$$

Here $Q = (\kappa - 1)(\Gamma_1^2 - \Gamma_2^2) + \Delta f_{\text{res}}[2S - (1 + \kappa)\Delta f_{\text{res}}]$, $S = \sqrt{\kappa(\Gamma_1^2 + \Gamma_2^2 + \Delta f_{\text{res}}^2) - \kappa^2 \Gamma_1^2 - \Gamma_2^2}$, $\Delta U_{\text{dc},1}, \Delta U_{\text{dc},2}$ are the total intrinsic fluctuations of the output dc voltages $U_{\text{dc},1}, U_{\text{dc},2}$ (noise voltages), respectively. Depending on the features of a particular experiment voltage fluctu-

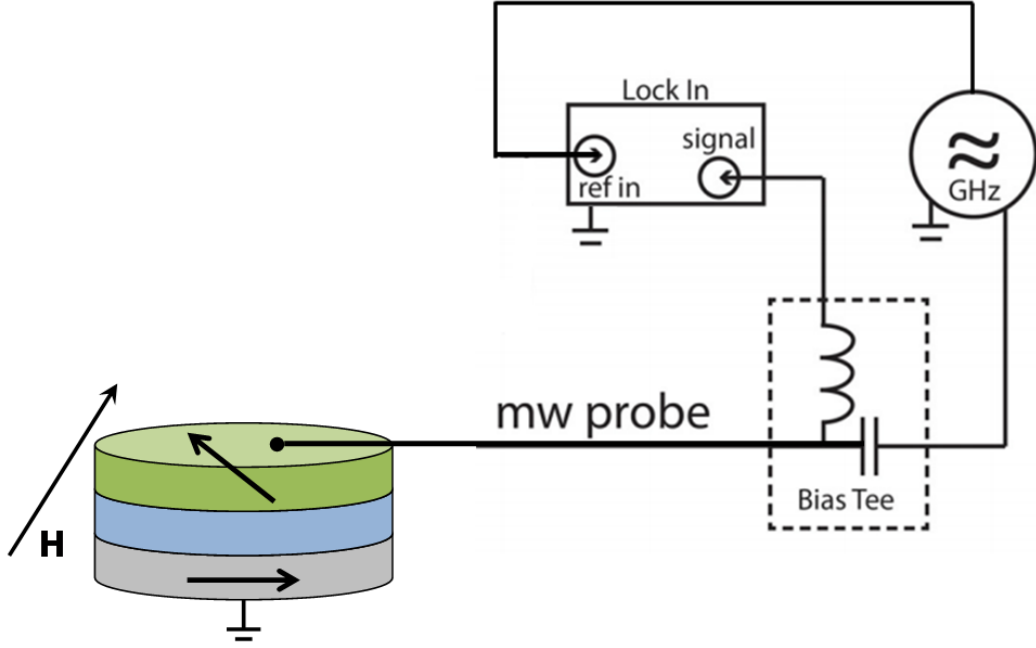


Figure 3.1: Schematic diagram of the amplitude-modulation ST-FMR setup.

ations $\Delta U_{\text{dc},1}$, $\Delta U_{\text{dc},2}$ may have contributions from a thermal noise, shot noise (important for a dc biased STMDs), flicker noise etc. For the most typical case of a passive STMD operating in the presence of a thermal noise the voltage fluctuations $\Delta U_{\text{dc},1}$ and $\Delta U_{\text{dc},2}$ can be calculated from Eq. (3) in Ref. [52] (see also [10] for details).

The equation (3.5) for Δf is complicated and nonlinearly depends on the detectors' parameters. In the discussion section it will be simplified and used for the explanation of our experimental data.

3.3 Experiment

Fig. 3.1 shows the schematic setup of our amplitude-modulated spin torque ferromagnetic resonance

(ST-FMR) [53, 54] measurement of an MTJ based microwave detector. In the experiment, the microwave generator applies a microwave current $I(t)$ to the MTJ via a bias-tee and a microwave probe. The generated STT drives the magnetization precession in the FL of an MTJ, leading to concurrent resistance oscillation $R(t)$ owing to the sample's TMR. The resistance oscillation $R(t)$ then rectifies with the microwave current $I(t)$ and produces a dc voltage U_{dc} . By keeping the external magnetic field applied to the MTJs constant and sweeping the microwave drive frequency f , the amplitude of this dc voltage signal U_{dc} changes accordingly and reaches extrema when certain resonant conditions are met. In order to improve the signal-to-noise ratio (SNR), lock-in detection technique was employed. We utilize a pair of uncoupled MTJ detectors as a detector array for precision frequency detection. In order to separately control the resonance frequencies of the two detectors, we can apply different external fields, $B_{dc,1}$ and $B_{dc,2}$ to the first and the second detector, respectively. Detailed description of the used experimental technique can be found in [54].

All MTJs discussed in this paper are of elliptical shape with both free and pinned layers in-plane magnetized. The sample stack structure is of the form: Substrate / SAF / MgO / FL / Cap (SAF: synthetic anti-ferromagnetic layer). The compositions of SAF and FL are PtMn(15) / Co₇₀Fe₃₀(2.5) / Ru(0.85) / Co₄₀Fe₄₀B₂₀(2.4), and Co₆₀Fe₂₀B₂₀(1.6–3.0), respectively (thicknesses in nanometers). In this paper, we discuss three detector arrays of different FL thicknesses: $l = 3.0$ nm [case (a)], $l = 2.3$ nm [case (b)], and $l = 1.6$ nm [case (c)].

In our experiment, ST-FMR was performed separately on each of the two uncoupled MTJ detectors inside the same detector array. The microwave power P_{rf} was carefully adjusted so that both detectors received nearly equal power. External dc magnetic field was applied

Table 3.1: The FL thicknesses l , applied external fields $B_{\text{dc},1}$, $B_{\text{dc},2}$ and delivered microwave power P_{rf} for the three detector arrays studied in the experiment (see Fig. 3.2)

Case	l , nm	$B_{\text{dc},1}$, G	$B_{\text{dc},2}$, G	P_{rf} , μW
(a)	3.0	-300	-700	1.51
(b)	2.3	-600	700	0.39
(c)	1.6	-900	1000	0.25

along MTJ FL hard axis in order to obtain the optimal volt-watt sensitivity ε_{res} [18]. The delivered microwave power P_{rf} and the applied external fields, $B_{\text{dc},1}$ and $B_{\text{dc},2}$, used in the experiment are summarized in table 3.1.

3.4 Results and Discussion

Fig. 3.2 summarizes the FMR measurement results of the three detector arrays: solid lines are the measured FMR curves, while dashed lines are the fitted curves calculated from Eq. (3.1). From these fitted curves we obtain the resonance frequencies $f_{\text{res},1}$ and $f_{\text{res},2}$, FMR linewidths Γ_1 and Γ_2 , and the resonance volt-watt sensitivities $\varepsilon_{\text{res},1}$ and $\varepsilon_{\text{res},2}$ for the three sets of detector arrays shown in table 3.2. The insets in Fig. 3.2 represent the discrepancy between the determined frequency f_{det} and real frequency f_{real} (frequency error $\Delta f = |f_{\text{det}} - f_{\text{real}}|$) as a function of the real frequency f_{real} , where f_{det} is calculated from Eq. (3.4) based on the measured frequency-dependent output dc voltages $U_{\text{dc},1}(f_{\text{real}})$, $U_{\text{dc},2}(f_{\text{real}})$ of the detectors and the fitting of the corresponding FMR signals using data from table 3.2.

When the microwave drive frequency falls between the resonances of the two detectors, the determined frequency error Δf is generally smaller than the FMR signal linewidths Γ_1 , Γ_2 (Fig. 3.3). In Fig. 3.3 orange, violet and green points show the dependence of the frequency error $\Delta f = |f_{\text{det}} - f_{\text{real}}|$ on the real microwave driven frequency f_{real} for the three mentioned cases of studied detector arrays: (a), (b) and (c), respectively (see table 3.1 for details). The

Table 3.2: The resonance frequencies $f_{\text{res},1}$ and $f_{\text{res},2}$ (in GHz units), FMR linewidths Γ_1 and Γ_2 (in GHz units), and resonance volt-watt sensitivities $\varepsilon_{\text{res},1}$ and $\varepsilon_{\text{res},2}$ (in mV/mW units) calculated from the fitted curves shown in Fig. 3.2 for the three detector arrays studied in the experiment

Case	$f_{\text{res},1}$	$f_{\text{res},2}$	Γ_1	Γ_2	$\varepsilon_{\text{res},1}$	$\varepsilon_{\text{res},2}$
(a)	4.810	6.515	0.199	0.202	5.30	5.97
(b)	4.242	5.813	0.218	0.248	28.20	17.72
(c)	5.419	6.019	0.232	0.148	35.71	59.21

values of Γ_1 and Γ_2 are shown in Fig. 3.3 by horizontal solid and dashed lines, respectively.

To explain the experimental results shown in Figs. 3.2 and 3.3 we make several simplifications of the theoretical model considered in the two STMD model. First, we assume that for both detector's noise voltages, $\Delta U_{\text{dc},1}$, $\Delta U_{\text{dc},2}$ in (3.5), have almost the same values and can be replaced with a single quantity $\Delta U_{\text{dc}} = \Delta U_{\text{dc},1} = \Delta U_{\text{dc},2}$. In general, this is not always the case. For instance, taking into account the existence of a thermal noise only, the noise voltages $\Delta U_{\text{dc},1}$, $\Delta U_{\text{dc},2}$ depend on the output dc voltages $U_{\text{dc},1}$, $U_{\text{dc},2}$ of the STMDs and the driving frequency [52]. On the other hand, in actual experiments there is always coupling between the closely-located detectors that causes a deviation of the detector's output voltages from the value given by Eq. (3.1), so this coupling manifests itself as effective frequency-dependent "coupling noise". Fully accounting this noise is a complicated task and, therefore, we employ a simplified approach in our analysis of the experimental data assuming the noise voltage ΔU_{dc} to be an adjustable parameter. This approximation gives good qualitative agreement between the experimental data (green points in Fig. 3.3) and theoretically calculated curve of Δf from Eq. (3.5) (black dash-dotted line in Fig. 3.3, $\Delta U_{\text{dc}} = 1 \mu\text{V}$) for the STMDs with closely-located resonance frequencies where one could neglect the frequency dependence of $\Delta U_{\text{dc},1}$ and $\Delta U_{\text{dc},2}$.

As one can see in Fig. 3.3, generally, the frequency error Δf decreases substantially in the range $f_{\text{res},1} + \Gamma_1 \leq f \leq f_{\text{res},2} - \Gamma_2$, while at frequencies f that close to the detector's

resonance frequencies it increases. This behavior can be explained by the effective increase of the SNR in the mentioned frequency range $f_{\text{res},1} + \Gamma_1 \leq f \leq f_{\text{res},2} - \Gamma_2$. In this case both output dc voltages $U_{\text{dc},1}$, $U_{\text{dc},2}$ of the detectors are similar and have values exceeding the voltage fluctuations $\Delta U_{\text{dc},1}$ and $\Delta U_{\text{dc},2}$. Thus, the contribution of the first and the second term under the square root in Eq. (3.5) are almost the same and the values of both terms are substantially less than 1 forcing a small value of the frequency error Δf . In contrast, at signal frequencies f that are very close to one of the detector's resonance frequencies ($f - f_{\text{res},1} < \Gamma_1$ or $f_{\text{res},2} - f < \Gamma_2$) the total SNR ratio of the microwave frequency detector decreases due to the deterioration of optimal work condition for both STMDs. As it follows from Eq. (3.5) (see also black dash-dotted curve in Fig. 3.3), the frequency error Δf increases if $U_{\text{dc},1} \gg U_{\text{dc},2}$ ($f \approx f_{\text{res},1}$) or $U_{\text{dc},1} \ll U_{\text{dc},2}$ ($f \approx f_{\text{res},2}$). This situation is similar to the case of a single detector operating in a frequency range near its resonance frequency, while a signal from the other detector acts like a weak additional noise signal that slightly pushes the first STMD from its optimal working point.

The advantages of the considered microwave frequency detector in the frequency range $f_{\text{res},1} + \Gamma_1 \leq f \leq f_{\text{res},2} - \Gamma_2$, however, disappear when previously introduced dimensionless parameter κ becomes approximately equal to 1 (the case of almost identical detectors) or when one of the detectors's output dc voltages becomes comparable to its noise voltage (so, the SNR becomes approximately equal to 1). For a system of two almost identical detectors (case (a) of the studied detectors arrays, see Fig. 3.2(a) and table 3.2), $\Gamma_1 \approx \Gamma_2$, $\varepsilon_{\text{res},1} \approx \varepsilon_{\text{res},2}$ and κ is close to 1 in almost the whole optimal frequency range $f_{\text{res},1} + \Gamma_1 \leq f \leq f_{\text{res},2} - \Gamma_2$, which leads to the substantial increase in the frequency error Δf and the proposed method of frequency determination becomes too inaccurate (see orange squares in Fig. 3.3). The considered frequency determination method also loses its efficiency when the difference between the resonance frequencies Δf_{res} becomes too large ($\Delta f_{\text{res}} \gg \Gamma_1 + \Gamma_2$) forcing a substantial decrease of the measured output dc voltages at frequencies far from the resonance frequencies of the detectors. In this case, the measured voltages could become comparable to the noise

voltages leading to the considerable decrease of the SNR of the system and the increase of the frequency error. Thus, a high-efficiency microwave frequency detector can be achieved in case of two STMDs having substantially different FMR linewidths and/or resonance volt-watt sensitivities, and closely-located resonance frequencies.

Furthermore, the analysis of data in Fig. 3.3 and numerical calculations based on Eq. (3.5) show that the frequency error decreases as the FL becomes thinner. The frequency error attributed to the enhanced resonance volt-watt sensitivity of an STMD for thinner FLs [18] (see table 3.2) and to the change of the voltage fluctuations $\Delta U_{dc,1}$, $\Delta U_{dc,2}$ (the performance of STMD operating in the presence of a thermal noise is considered in Refs. [52, 10]). As one can see from Fig. 3.3, the frequency determination error Δf reduces approximately by a factor of 3 when the FL thickness l decreases from 3 nm to 1.6 nm. This result can be useful for the development and optimization of high-accuracy microwave frequency detectors.

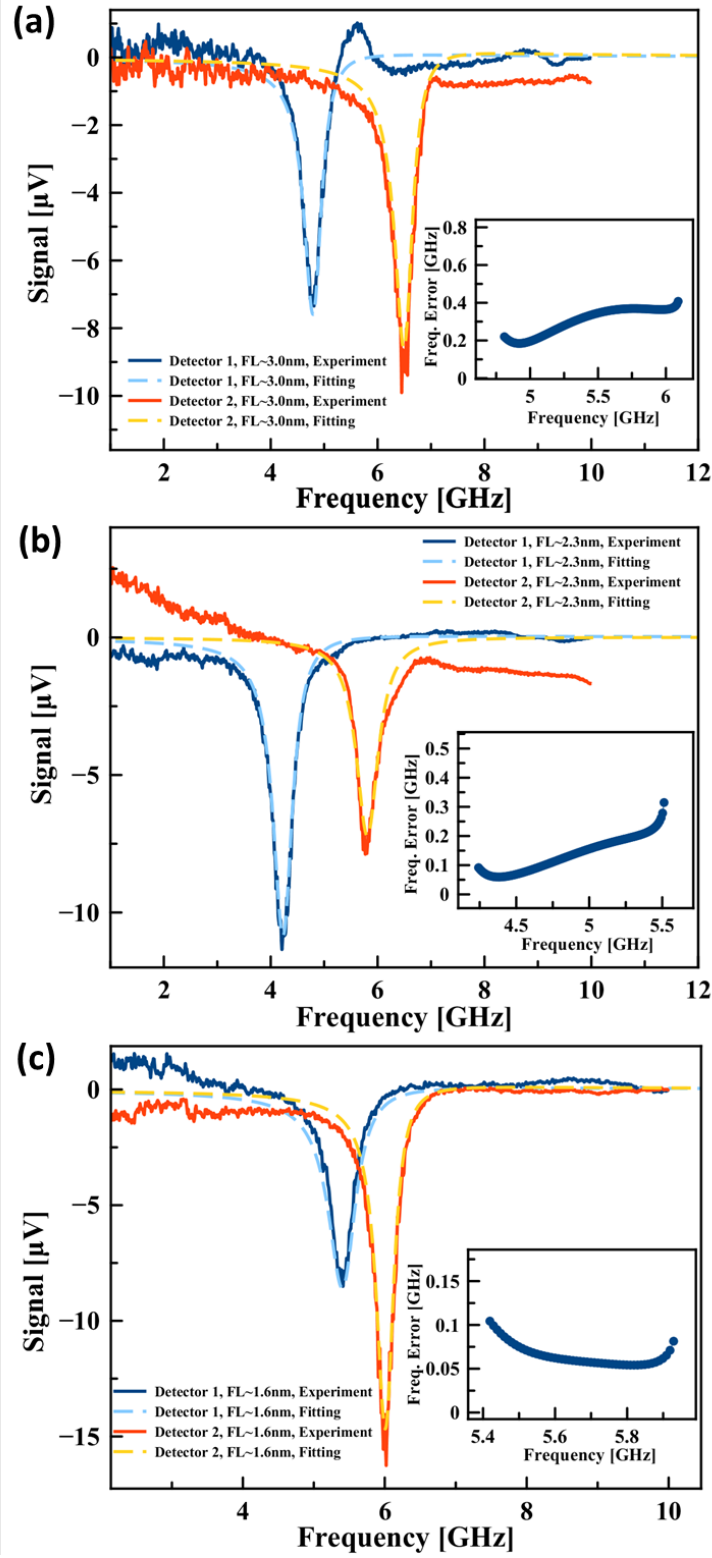


Figure 3.2: Measured FMR signals (solid lines) and fitted curves (dashed lines) versus microwave drive frequency for three sets of detector arrays of different FL thicknesses: (a) $l = 3.0$ nm, (b) $l = 2.3$ nm, and (c) $l = 1.6$ nm. The insets show the determined frequency error Δf as a function of the drive frequency.

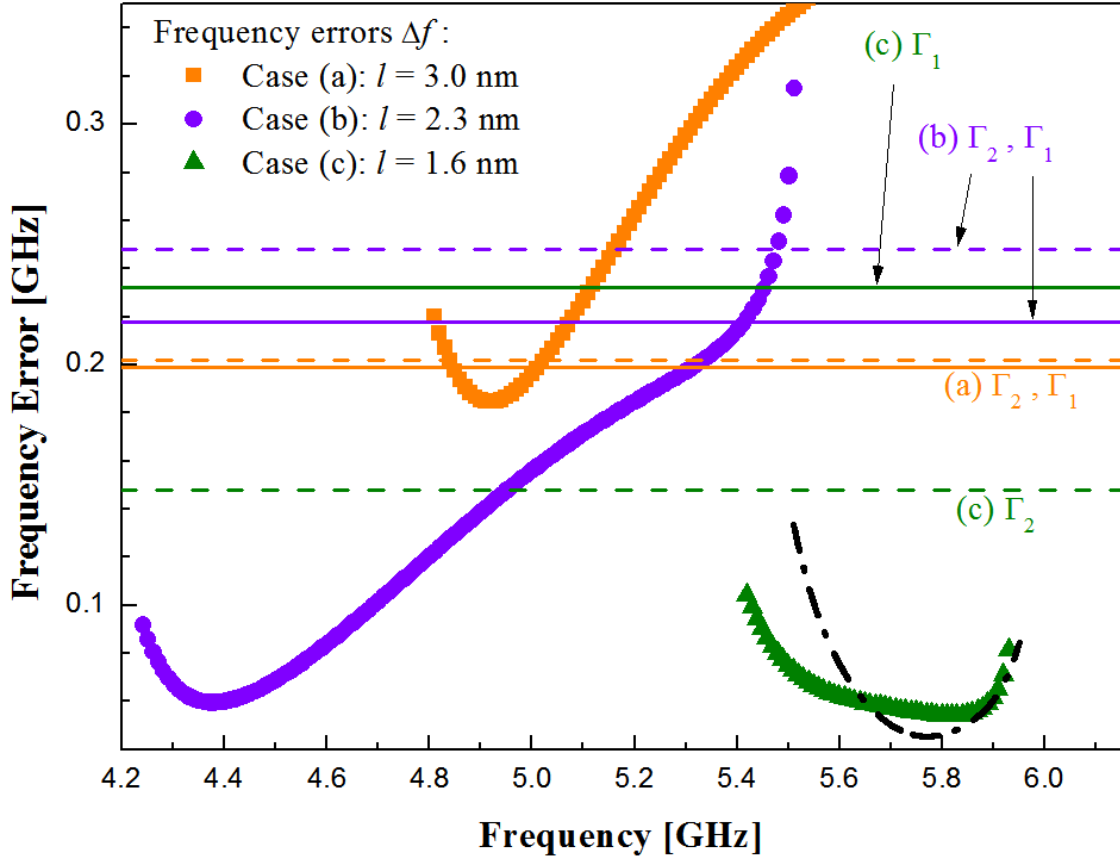


Figure 3.3: Frequency errors $\Delta f = |f_{\text{det}} - f_{\text{real}}|$ (color points) calculated from the determined frequency f_{det} [given by Eq. (3.4)] and real frequency f_{real} as a function of microwave drive frequency f_{real} for three studied cases of detector arrays: (a) orange squares, (b) violet circles, and (c) green triangles. The values of the detector's FMR linewidths for three detector arrays are indicated by color-coded solid (Γ_1) and dashed (Γ_2) horizontal lines, respectively. Black dash-dotted line is the theoretically calculated dependence Δf from Eq. (3.5) for the third detector array (c).

Chapter 4

Conclusion

In the first part of this thesis, we have shown a successful design of a compact, ruggedized, and ESD-protected microwave radiation detector using magnetic tunnel junctions as sensing elements. The detection frequency range of this MTJ-based radiation detector can be tuned via adjusting the magnet installed inside. Besides this additional feature, the detector's sensitivity (240 mV/mW) under zero current bias is comparable with that of current Schottky diode detectors. We have also shown that MTJ samples with larger perpendicular anisotropy of free layers performed with better sensitivity than in-plane MTJs. This improvement is due to the voltage induced anisotropy. To achieve wider range detection function, detectors with two parallel MTJs were assembled, which can detect two different ranges of microwave signals simultaneously. The first-hand experimental results provided robustness and reliability for application purpose.

For further performance enhancement, active dc biased detectors can be considered since i) the voltage induced anisotropy can be more effective and ii) the effective damping can be reduced by the current induced spin transfer torque[23]. In addition to the improvements on the MTJ sensing elements, better impedance matching between the air, the antenna, and

the sensing element using a more optimized circuit design will also be helpful. On the other hand, more investigation on the noise properties of these detectors is desired as it is another crucial factor for further increasing the sensitivity.

The second project describes an effective approach for reducing the error in detecting the frequency of the microwave signal based on two uncoupled STMDs connected in parallel to a microwave signal source. This method is applicable for the signals of unknown microwave power and could determine the frequency with an error substantially smaller than the detector's FMR linewidth. In both theoretical and experimental work, we demonstrated that when the two thin-free-layer STMDs have similar resonance frequencies, but different FMR linewidths and resonance volt-watt sensitivities, the accuracy of microwave frequency detection will be improved compared to a single STMD based detector.

Bibliography

- [1] G. E. Rowlands. Stochastic magnetic dynamics in patterned nanostructures. *PhD thesis*, 2012.
- [2] D. C. Ralph and M. D. Stiles. Spin transfer torques. *Journal of Magnetism and Magnetic Materials*, 320:1190–1216, 2008.
- [3] J. C. Slonczewski. Conductance and exchange coupling of two ferromagnets separated by a tunneling barrier. *Physical Review B*, 39:6995, 1989.
- [4] W. H. Butler, X. G. Zhang, T. C. Schulthess, and etc. Spin-dependent tunneling conductance of fe—mgo—fe sandwiches. *Physical Review B*, 63:054416, 2001.
- [5] J. Mathon and A. Umerski. Theory of tunneling magnetoresistance of an epitaxial fe/mgo/fe(001) junction. *Physical Review B*, 63:220403, 2001.
- [6] S. P. Parkin, C. Kaiser, A. Panchula, and etc. Giant tunnelling magnetoresistance at room temperature with mgo (100) tunnel barriers. *Nature Materials*, 3:862, 2004.
- [7] J. Hayakawa, S. Ikeda, F. Matsukura, and etc. Dependence of giant tunnel magnetoresistance of sputtered cofeb/mgo/cofeb magnetic tunnel junctions on mgo barrier thickness and annealing temperature. *Japanese Journal of Applied Physics*, 44:16, 2005.
- [8] H. X. Wei, Q. H. Qin, M. Ma, and etc. 80% tunneling magnetoresistance at room temperature for thin al—o barrier magnetic tunnel junction with cofeb as free and reference layers. *Journal of Applied Physics*, 101:09B501, 2007.
- [9] S. Ikeda, J. Hayakawa, Y. Ashizawa, and etc. Tunnel magnetoresistance of 604% at 300k300k by suppression of ta diffusion in cofeb/mgo/cofebcofeb/mgo/cofeb pseudo-spin-valves annealed at high temperature. *Applied Physics Letters*, 93:082508, 2008.
- [10] O. V. Prokopenko, I. N. Krivorotov, T. J. Meitzler, E. Bankowski, V. S. Tiberkevich, and A. N. Slavin. Spin-torque microwave detectors. *Magnonics: From Fundamentals to Applications*, 125, 2013.
- [11] M. Julliere. Tunneling between ferromagnetic films. *Phys. Lett. A*, 54:225, 1975.
- [12] S. Yuasa, T. Nagahama, A. Fukushima, Y. Suzuki, and K. Ando. Giant room-temperature magnetoresistance in single-crystal fe/mgo/fe magnetic tunnel junctions. *Nature Mater.*, 3:868, 2004.

- [13] S. Ikeda, K. Miura, H. Yamamoto, K. Mizunuma, H. D. Gan, and etc. A perpendicular-anisotropy cofeb–mgo magnetic tunnel junction. *Nature Mater.*, 9:721, 2010.
- [14] J. C. Slonczewski. Current-driven excitation of magnetic multilayers. *J. Magn. Magn. Mater.*, 159, 1996.
- [15] L. Berger. Emission of spin waves by a magnetic multilayer traversed by a current. *Phys. Rev. B*, 54:9353, 1996.
- [16] A. A. Tulapurkar, Y. Suzuki, A. Fukushima, H. Kubota, H. Maehara, and etc. Spin-torque diode effect in magnetic tunnel junctions. *Nature*, 438:339, 2005.
- [17] J. C. Sankey, P. M. Braganca, A. G. F. Garcia, I. N. Krivorotov, R. A. Buhrman, and D. C. Ralph. Spin-transfer-driven ferromagnetic resonance of individual nanomagnets. *Phys. Rev. Lett.*, 96:227601, 2006.
- [18] C. Wang, Y. T. Cui, J. Z. Sun, K. Mizunuma, and etc. Sensitivity of spin-torque diodes for frequency-tunable resonant microwave detection. *Journal of Applied Physics*, 106:053905, 2009.
- [19] X. Fan, R. Cao, T. Moriyama, and etc. Magnetic tunnel junction based microwave detector. *Applied Physics Letters*, 95:122501, 2009.
- [20] S. Ishibashi, T. Seki, T. Nozaki, and etc. Large diode sensitivity of cofeb/mgo/cofeb magnetic tunnel junctions. *Applied Physics Express*, 3:073001, 2010.
- [21] O. V. Prokopenko, I. N. Krivorotov, E. Bankowski, and etc. Spin-torque microwave detector with out-of-plane precessing magnetic moment. *Journal of Applied Physics*, 111:123904, 2012.
- [22] O. V. Prokopenko and A. N. Slavin. Microwave detectors based on the spin-torque diode effect. *Low Temperature Physics*, 41:353, 2015.
- [23] S. Miwa, S. Ishibashi, H. Tomita, and etc. Highly sensitive nanoscale spin-torque diode. *Nature Materials*, 13:3778, 2013.
- [24] X. Cheng, C. T. Boone, J. Zhu, and I. N. Krivorotov. Nonadiabatic stochastic resonance of a nanomagnet excited by spin torque. *Phys. Rev. Lett.*, 105:047202, 2010.
- [25] M. T. Johnson, P. J. H. Bloemen, F. J. A. den Broeder, and etc. Magnetic anisotropy in metallic multilayers. *Journal of Applied Physics*, 59:11, 1996.
- [26] R. L. Stamps, L. Louail, M. Hehn, and etc. Anisotropies, cone states, and stripe domains in co/pt multilayers. *Journal of Applied Physics*, 81:8, 1998.
- [27] J. C. Slonczewski. Currents, torques, and polarization factors in magnetic tunnel junctions. *Phys. Rev. B*, 71:1–10, 2005.
- [28] G. Binasch and P. Grünberg. Enhanced magnetoresistance in layered magnetic structures with antiferromagnetic interlayer exchange. *Phys. Rev. B*, 39:4828–4830, 1989.

- [29] M. Baibich and J. Broto. Giant magnetoresistance of (001) Fe/(001) Cr magnetic superlattices. *Phys. Rev. Letters*, 61:2472–2475, 1988.
- [30] J. Slonczewski. Currents and torques in metallic magnetic multilayers. *Journal of magnetism and magnetic materials*, 247:324–338, 2002.
- [31] B. Oliver, Q. He, X. Tang, and J. Nowak. Dielectric breakdown in magnetic tunnel junctions having an ultrathin barrier. *J. Appl. Phys.*, 91:4348, 2002.
- [32] J. C. Slonczewski and J. Z. Sun. Theory of voltage-driven current and torque in magnetic tunnel junctions. *J. Magn. Magn. Mater.*, 310:169–175, 2007.
- [33] I. Theodonis, N. Kioussis, A. Kalitsov, and etc. Anomalous bias dependence of spin torque in magnetic tunnel junctions. *Phys. Rev. Letters*, 97:237205, 2006.
- [34] S. I. Kiselev, J. C. Sankey, I. N. Krivorotov, and etc. Microwave oscillations of a nanomagnet driven by a spin polarized current. *Nature*, 425:380–3, 2003.
- [35] W. H. Rippard, M. R. Pufall, S. Kaka, and etc. Direct-current induced dynamics in Co₉₀Fe₁₀/Ni₈₀Fe₂₀ point contacts. *Phys. Rev. Letters*, 92:90–93, 2004.
- [36] J. A. Katine, F. J. Albert, R. A. Buhrman, and etc. Current driven magnetization reversal and spin-wave excitations in Co/Cu/Co pillars. *Phys. Rev. Letters*, 84:3149–52, 2000.
- [37] C. Kittel. On the theory of ferromagnetic resonance absorption. *Physical Review*, 73:155–161, 1948.
- [38] B. K. Kuanr, R. E. Camley, Z. Celinski, and etc. Extrinsic contribution to Gilbert damping in sputtered NiFe films by ferromagnetic resonance. *Journal of Magnetism and Magnetic Materials*, 286:276–281, 2005.
- [39] J. Sankey and etc. Measurement of the spin-transfer-torque vector in magnetic tunnel junctions. *Nature Physics*, 4:67–71, 2008.
- [40] D. D. Djayaprawira, K. Tsunekawa, M. Nagai, and etc. 230% room-temperature magnetoresistance in CoFeB/MgO/CoFeB/MgO/CoFeB magnetic tunnel junctions. *Applied Physics Letters*, 86:092502, 2005.
- [41] R. N. Simons. Coplanar waveguide circuits components systems. *Wiley-IEEE Press*, 2001.
- [42] J. Xiao, G. E. W. Bauer, and A. Brataas. Spin-transfer torque in magnetic tunnel junctions: Scattering theory. *Phys. Rev. B*, 77:224419, 2008.
- [43] T. Maruyama, Y. Shiota, T. Nozaki, and etc. Large voltage-induced magnetic anisotropy change in a few atomic layers of iron. *Nature Nanotechnology*, 4:158 – 161, 2009.
- [44] T. Nozaki, Y. Shiota, M. Shiraishi, and etc. Voltage-induced perpendicular magnetic anisotropy change in magnetic tunnel junctions. *Appl. Phys. Lett.*, 96:022506, 2010.

- [45] Y. Shiota, S. Murakami, F. Bonell, and etc. Quantitative evaluation of voltage-induced magnetic anisotropy change by magnetoresistance measurement. *Applied Physics Express*, 4:4, 2011.
- [46] H. Kubota, S. Ishibashi, T. Saruya, and etc. Enhancement of perpendicular magnetic anisotropy in feb free layers using a thin mgo cap layer. *J. Appl. Phys.*, 07C723:111, 2012.
- [47] K. Yamada, H. Kakizakai, K. Shimamura, and etc. Electric field modulation of magnetic anisotropy in mgo/co/pt structure. *Applied Physics Express*, 6:7, 2013.
- [48] J. Zhu, J. A. Katine, G. E. Rowlands, and etc. Voltage-induced ferromagnetic resonance in magnetic tunnel junctions. *Phys. Rev. Lett.*, 108:197203, 2012.
- [49] B. Fang, M. Carpentieri, X. Hao, and etc. Giant spin-torque diode sensitivity in the absence of bias magnetic field. *Nature Communications*, 7:11259, 2016.
- [50] X. Cheng, J. A. Katine, G. E. Rowlands, and I. N. Krivorotov. Nonlinear ferromagnetic resonance induced by spin torque in nanoscale magnetic tunnel junctions. *Appl. Phys. Lett.*, 103:082402, 2013.
- [51] A. G. Gurevich and G. A. Melkov. Magnetization oscillations and waves. *CRC Press, New York*, 1996.
- [52] O. Prokopenko, G. Melkov, E. Bankowski, and etc. Noise properties of a resonance-type spin-torque microwave detector. *Appl. Phys. Lett.*, 99:032507, 2011.
- [53] C. Wang, Y.-T. Cui, J. A. Katine, and etc. Time-resolved measurement of spin-transfer-driven ferromagnetic resonance and spin torque in magnetic tunnel junctions. *Nature Physics*, 7:496–501, 2011.
- [54] A. M. Gonçalves, I. Barsukov, Y.-J. Chen, and etc. Time-resolved measurement of spin-transfer-driven ferromagnetic resonance and spin torque in magnetic tunnel junctions. *Appl. Phys. Lett.*, 103:172406, 2013.